

Article

Direct-bandgap emission from hexagonal Ge and SiGe alloys

<https://doi.org/10.1038/s41586-020-2150-y>

Received: 25 October 2019

Accepted: 11 February 2020

Published online: 8 April 2020

 Check for updates

Elham M. T. Fadaly^{1,7}, Alain Dijkstra^{1,7}, Jens René Suckert^{2,7}, Dorian Ziss³, Marvin A. J. van Tilburg¹, Chenyang Mao¹, Yizhen Ren¹, Victor T. van Lange¹, Ksenia Korzun¹, Sebastian Kölling^{1,6}, Marcel A. Verheijen^{1,4}, David Busse⁵, Claudia Rödl², Jürgen Furthmüller², Friedhelm Bechstedt², Julian Stangl³, Jonathan J. Finley⁵, Silvana Botti², Jos E. M. Haverkort¹ & Erik P. A. M. Bakkers^{1,8}

Silicon crystallized in the usual cubic (diamond) lattice structure has dominated the electronics industry for more than half a century. However, cubic silicon (Si), germanium (Ge) and SiGe alloys are all indirect-bandgap semiconductors that cannot emit light efficiently. The goal¹ of achieving efficient light emission from group-IV materials in silicon technology has been elusive for decades^{2–6}. Here we demonstrate efficient light emission from direct-bandgap hexagonal Ge and SiGe alloys. We measure a sub-nanosecond, temperature-insensitive radiative recombination lifetime and observe an emission yield similar to that of direct-bandgap group-III–V semiconductors. Moreover, we demonstrate that, by controlling the composition of the hexagonal SiGe alloy, the emission wavelength can be continuously tuned over a broad range, while preserving the direct bandgap. Our experimental findings are in excellent quantitative agreement with ab initio theory. Hexagonal SiGe embodies an ideal material system in which to combine electronic and optoelectronic functionalities on a single chip, opening the way towards integrated device concepts and information-processing technologies.

Silicon has been the workhorse of the semiconductor industry because of its many highly advantageous physical, electronic and technological properties. However, owing to its indirect bandgap, silicon cannot emit light efficiently—a property that has seriously constrained its applications to electronics and passive optical circuitry^{7–9}. Silicon technology can only reach its full application potential when supplemented¹⁰ with an efficient, direct-bandgap light emitter.

The band structure of cubic (cub-)Si, presented in Fig. 1a, is very well known, having the lowest conduction-band minimum close to the high-symmetry X-point and a second-lowest minimum at the L-point. As such, it is the archetypal example of an indirect-bandgap semiconductor, which, despite many efforts^{2–5}, cannot be used for efficient light emission. By modifying the crystal structure from cubic to hexagonal, the symmetry along the <111> crystal direction changes fundamentally, with the consequence that the L-point bands are folded back onto the Γ -point. As shown in Fig. 1b, for hexagonal (hex-)Si, this results in a local conduction-band minimum at the Γ -point, with an energy close to 1.7 eV (refs. ^{11–13}). Clearly, the bandgap of hex-Si remains indirect because the lowest-energy conduction-band minimum is at the M-point, close to 1.1 eV. Cub-Ge also has an indirect bandgap but, unlike Si, its lowest conduction-band minimum is situated at the L-point, as shown in Fig. 1c. As a consequence, for hex-Ge the band-folding effect results in a direct bandgap at the Γ -point with a magnitude close to 0.3 eV, as shown in the calculated band structure in Fig. 1d¹⁴.

To investigate how the direct bandgap energy can be tuned by alloying Ge with Si, we calculated the band structures of hex-Si_{1-x}Ge_x (for $0 < x < 1$) using ab initio density functional theory (DFT) and a cluster expansion method for isostructural hexagonal binary alloys (see Methods for details). Selected results of our calculations, presented in Fig. 1e, show the composition-dependent size of the emission bandgap for random hex-Si_{1-x}Ge_x alloys at high-symmetry points in the Brillouin zone. Clearly, a direct bandgap is predicted at the Γ -point for $x > 0.65$ (red curve) with a magnitude that is tunable across the energy range 0.3–0.7 eV. This spectral interval is of technological interest for many potential applications including optical interconnects in computing^{15,16}, silicon quantum photonic circuits⁸ and optical sensing^{17,18}, among others^{19,20}. Figure 1f shows the calculated radiative lifetime of 10^{19} cm⁻³ n-doped hex-Si_{1-x}Ge_x alloys for different compositions. Remarkably, the radiative lifetimes of hex-Si_{1-x}Ge_x alloys are substantially lower than that of pure hex-Ge, for which the lowest-energy transition is dipole forbidden at the Γ -point¹⁴. This observation can be traced to the reduced symmetry in the random hex-Si_{1-x}Ge_x alloys, which leads to mixing of Ge s-states into the lowest conduction-band wavefunction. We note that the calculated lifetimes of the hex-Si_{1-x}Ge_x alloys are approaching those of semiconductors from groups III–V of the periodic table, such as GaAs. Ge-rich alloys of hex-Si_{1-x}Ge_x are thus highly appealing because they are theoretically predicted to combine a direct bandgap, strong optical transitions and wavelength tunability.

¹Department of Applied Physics, Eindhoven University of Technology, Eindhoven, The Netherlands. ²Institut für Festkörpertheorie und -optik, Friedrich-Schiller-Universität Jena, Jena, Germany.

³Institute of Semiconductor and Solid-State Physics, Johannes Kepler University, Linz, Austria. ⁴Eurofins Materials Science Netherlands, Eindhoven, The Netherlands. ⁵Physik Department & Walter-Schottky-Institut, Technische Universität München, Garching, Germany. ⁶Present address: Department of Engineering Physics, École Polytechnique de Montréal, Montreal, Québec, Canada. ⁷These authors contributed equally: Elham M. T. Fadaly, Alain Dijkstra, Jens René Suckert. [✉]e-mail: e.p.a.m.bakkers@tue.nl

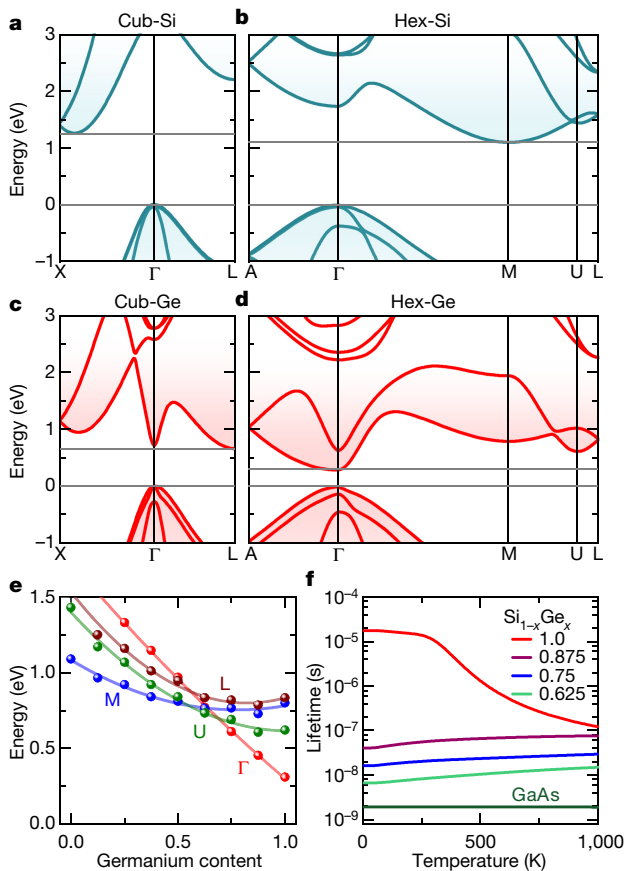


Fig. 1 | Calculated band structure of hex-Si_{1-x}Ge_x. **a–d**, Band structures of cub-Si (**a**), hex-Si (**b**), cub-Ge (**c**) and hex-Ge (**d**) based on DFT calculations. **e**, Minimum conduction-band energy for the selected high-symmetry points Γ , M, L and U on the M–L line, fitted with parabolae as a function of the Ge content in the hex-Si_{1-x}Ge_x alloy. **f**, Radiative lifetime of different hex-Si_{1-x}Ge_x compositions for recombination events, with n-doping of 10^{19} cm⁻³, as compared to the radiative lifetime of cub-GaAs.

Here we demonstrate experimentally that Ge-rich alloys of hex-Si_{1-x}Ge_x are indeed direct-bandgap semiconductors, and we observe strong emission and a temperature-independent nanosecond radiative lifetime. Our results are shown to be in remarkable quantitative agreement with theoretical predictions.

We begin by discussing the growth and crystalline properties of hex-Si_{1-x}Ge_x alloys. Various methods have been proposed to grow hex-Si or hex-Ge including vapour–liquid–solid nanowire growth and strain-induced crystal transformation^{21–25}. Recently, high-quality Si-rich hex-Si_{1-x}Ge_x alloys have been grown using the crystal transfer method^{26,27} in which a wurtzite gallium phosphide (GaP) core nanowire is used as a template for the growth of hex-Si_{1-x}Ge_x because it is lattice-matched to Si. Here we grow Ge-rich Si_{1-x}Ge_x alloys around a thin (about 35 nm in diameter) wurtzite gold (Au) catalysed gallium arsenide (GaAs) core that is lattice-matched to Ge on a GaAs (111)B substrate, as shown in Fig. 2a. We use a thin GaAs core to further reduce lattice strain and strain-induced defects. The Au catalytic particles used to grow the wurtzite GaAs nanowire template were removed by wet chemical etching and thick (200–400 nm) Ge shells were grown epitaxially on the wurtzite-GaAs (see Methods and Extended Data Fig. 1a–d). The overview scanning electron microscopy image presented in Fig. 2b demonstrates that arrays of hex-GaAs/Ge-core/shell nanowires are formed on the growth substrate. These nanowires are uniform in length and diameter and have smooth, well defined {110} side facets indicative of a single crystalline nature (see Extended Data Fig. 1e). Figure 2c shows a

cross-sectional electron dispersive X-ray (EDX) spectroscopy map confirming the expected core/shell geometry. The high-resolution high-angular annular dark field (HAADF) transmission electron microscopy (TEM) image presented in Fig. 2d confirms the high-quality epitaxial growth of the Ge shell on the GaAs core and reveals an ABAB stacking along [0001], which is the hallmark of a hexagonal crystal structure. The crystal quality and lattice parameters of a range of samples with GaAs/Si_{1-x}Ge_x (with $x > 0.5$) core/shell wires were studied by X-ray diffraction (XRD) measurements using synchrotron radiation. Figure 2e shows a set of asymmetrical reciprocal space maps (RSMs) for samples with Si_{1-x}Ge_x shells with nominal Ge compositions $x = 1.00$, 0.92, 0.86, 0.74 and 0.61, respectively. The RSMs show the shift of the (1018) reflection that is exclusively permitted in the hexagonal crystal phase, as a function of the Ge concentration. The higher the Ge concentration, the more the hexagonal reflection shifts to lower $Q_{\text{out-of-plane}}$ and $Q_{\text{in-plane}}$ values, indicating an increase in the out-of-plane lattice parameter c and the in-plane lattice parameter a . From the narrow peak width along $Q_{\text{out-of-plane}}$, we can conclude that the overall crystal quality is very high, with an estimated stacking-fault density of 2–4 stacking faults per micrometre along the crystalline [0001] direction (for details see Methods). These results are in good agreement with the TEM measurements performed for the same samples (see Extended Data Fig. 2). To further confirm the high crystal quality of the samples, an asymmetric crystal-truncation-rod scan in combination with a polar scan for Si_{0.20}Ge_{0.80} composition is shown in Extended Data Fig. 5. We determine the lattice parameters a and c from a set of symmetric and asymmetric RSMs as a function of the Ge composition (see Methods). The results of these experiments are presented in Fig. 2f and Extended Data Fig. 4. Data points with $x > 0.7$ lie on the linear interpolation line between hex-Si and Ge (following Vegard's rule) indicating that the lattice strain in the Si_{1-x}Ge_x shell is negligible (more data is presented in Extended Data Fig. 4g). These observations unequivocally confirm the single-crystal nature of the nanowires and their hexagonal crystal structure.

We explore the optical properties of the hex-Si_{1-x}Ge_x nanowires probed using power- and temperature-dependent photoluminescence spectroscopy (Fig. 3a, b). We focus on two samples—pure hex-Ge as the binary endpoint of the hex-Si_{1-x}Ge_x alloy and Si_{0.20}Ge_{0.80} as being representative of the binary alloy in the middle of the compositional range for which a direct bandgap is expected. Figure 3a presents power-dependent photoluminescence spectra recorded at a temperature of 4 K. The spectrum obtained from the hex-Ge sample exhibits a narrow emission peak at the lowest excitation level investigated. Excitonic effects are not observed, owing to degenerate n-type doping (see Methods and Extended Data Fig. 6). As the excitation density is increased, the emission peak broadens towards high energies and the peak blueshifts by 19 meV. To understand the recombination mechanism, we have fitted both the excitation- and temperature-dependent data with the Lasher–Stern–Würfel (LSW) model^{28,29}, which describes band-to-band recombination in a semiconductor. Model fits are included in Fig. 3a, b, and confirm that the observed spectra of hex-Ge can be explained by a band-to-band recombination process. From the fits, it can be concluded that the high energy broadening is due to an increase in the electron temperature and the observed blueshift is due to the Burstein–Moss³⁰ effect. In comparison to the pure hex-Ge sample, the linewidth of the hex-Si_{0.20}Ge_{0.80} sample is larger owing to alloy broadening (60 meV compared to 14 meV for hex-Ge, at the lowest excitation density) and can therefore not be fitted by the LSW model. Only a slight excitation-induced blueshift of 6 meV was observed for the Si_{0.20}Ge_{0.80} sample. Figure 3b shows temperature-dependent photoluminescence spectra recorded from the hex-Ge and Si_{0.20}Ge_{0.80} sample. Clear asymmetric broadening is observed at high temperatures, which, from the LSW model fits, can be assigned to broadening of the Fermi–Dirac distribution tail, supporting our contention that the observed emission peak is due to a band-to-band recombination process. The bandgap of hex-Ge shifts from 3.5 μm (0.353 eV) at low

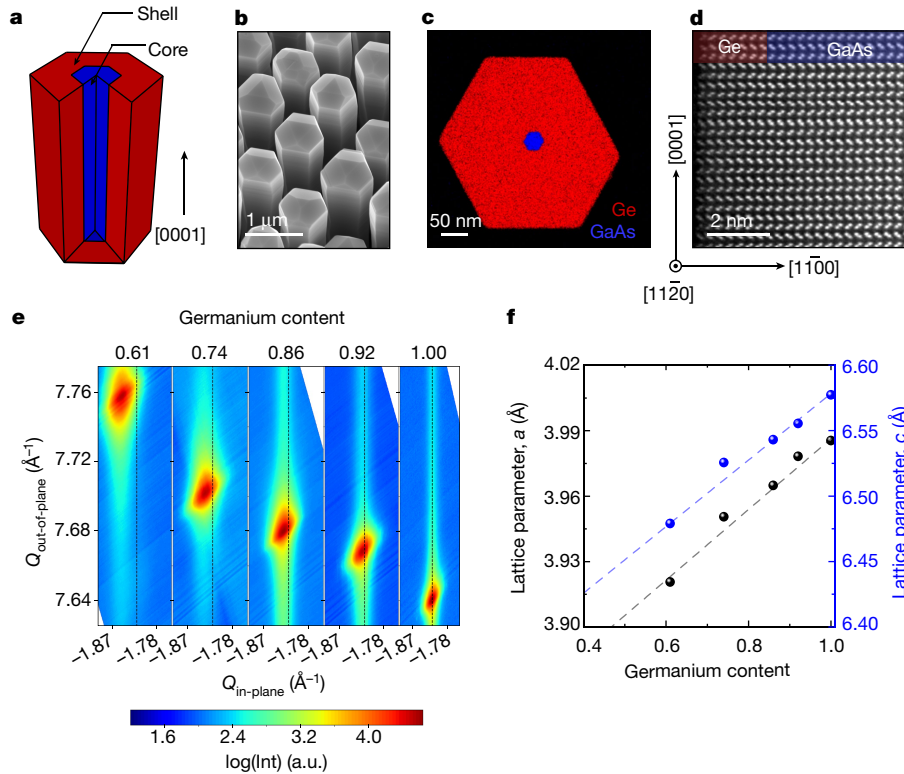


Fig. 2 | Overview of the hex- $\text{Si}_{1-x}\text{Ge}_x$ material system. **a**, Schematic illustration of the hexagonal GaAs/Ge core/shell nanowires drawn in blue/red, respectively. **b**, Tilted-view scanning electron micrograph of an array of epitaxial GaAs/Ge nanowires grown on a GaAs (111)B substrate in the [0001] crystallographic direction. **c**, HAADF-STEM and EDX overlapped images of a cross-sectional lamella of a representative GaAs/Ge core/shell nanowire. **d**, Aberration-corrected HAADF-STEM image of the interface of GaAs/Ge structure obtained in the [1120] zone axis, displaying the ABAB stacking along [0001] of the hexagonal crystal structure. **e**, X-ray diffraction reciprocal space maps showing the logarithmic scattering intensity (Int) of $Q_{\text{out-of-plane}}$ versus $Q_{\text{in-plane}}$ in arbitrary units (a.u.), around the hexagonal (1018) nanowire reflections shown for five different Ge concentrations. **f**, A plot of the hex- $\text{Si}_{1-x}\text{Ge}_x$ in-plane lattice parameter a and out-of-plane lattice parameter c as a function of the Ge content; the error bars are smaller than the data symbols (black and blue dots) used in the plot (see Extended Data Fig. 4g for more details). The composition of hex- $\text{Si}_{1-x}\text{Ge}_x$ crystals with $x=1.00$, 0.92 and 0.74 was determined by EDX-STEM and atom probe tomography (APT) as shown in Extended Data Fig. 4g and Extended Data Fig. 6. The other compositions, $x=0.86$ and 0.61, were determined based on interpolation.

temperature towards 4.4 μm (0.28 eV) at room temperature, confirming the expected bandgap shrinkage for a band-to-band transition, as depicted in Fig. 3c. The shrinkage of the $\text{Si}_{0.20}\text{Ge}_{0.80}$ bandgap as well as a detailed fit to the data of hex-Ge, which yield a Debye temperature of 66 K, is discussed in Methods. Figure 3d shows the temperature dependence of the integrated emission intensity of the samples on an Arrhenius representation. A decrease (by a factor of 15–100) of the integrated emission intensity is observed upon increasing the lattice temperature. The ratio of the photoluminescence emission intensity at 4 K and 300 K compares favourably to many well developed III–V semiconductors (see Methods).

The decrease of the intensity with increasing temperature is suppressed for higher excitation powers, as shown in Fig. 3d, owing to saturation of non-radiative processes. That the emission decreases with increasing temperature provides the first indication that hex-Ge is a direct-bandgap semiconductor. In contrast, for an indirect-bandgap semiconductor at low temperature, excited carriers accumulate at the indirect band extrema and do not, therefore, emit light efficiently. As the lattice temperature increases, the photoluminescence intensity is expected to increase³¹ as carriers are thermally excited into the higher-energy direct minimum, from where they can recombine with a higher quantum efficiency.

We next deduce the radiative lifetime as well as the radiative emission efficiency of hex- $\text{Si}_{0.20}\text{Ge}_{0.80}$. It is important to note that the measured decay lifetime is determined by the fastest recombination process, which can be either radiative or non-radiative in nature. It is therefore crucial to choose experimental conditions in which the measured recombination lifetime is exclusively governed by pure radiative recombination. To reach the radiative limit, we measure at low temperature, since non-radiative processes are usually thermally activated (see Methods). Moreover, we use a pulsed laser at high excitation density in order to saturate nonradiative processes. These experimental conditions are sufficient to reach the radiative limit, as will become clear when we discuss the temperature dependence of the emission intensity. Typical results from time-resolved luminescence measurements on a single wire from the $\text{Si}_{0.20}\text{Ge}_{0.80}$ sample are presented in Fig. 4a as a function

of temperature. We observe a clear mono-exponential decay transient, characteristic of a single, dominant decay channel. For all hex- $\text{Si}_{1-x}\text{Ge}_x$ nanowires investigated, the characteristic recombination lifetime is around 1 ns, very similar to conventional direct-bandgap semiconductors such as GaAs or InP at low temperatures with similar doping levels (see Methods). We observe that the experimentally obtained lifetime is an order of magnitude smaller than the theoretically calculated lifetime, which indicates that perfect crystal symmetry is also broken by other factors¹⁴. The left panels of Fig. 4b, c show the temperature dependence of both the recombination lifetime and the integrated emission intensity as a function of temperature from single wires from three different samples with varying dimensions and quality (see Extended Data Fig. 8b for more details). The wires show comparable lifetimes at low temperature, but the intensity and lifetime both start to decrease at a temperature of around 40 K (100 K) for sample III (II), which is the low-(medium-) quality wire. For the higher-quality sample, we observe a constant integrated photoluminescence intensity and lifetime as a function of temperature up to 220 K, which conclusively shows the absence of non-saturated thermally activated non-radiative recombination processes. Given that it is highly improbable that nonradiative losses are already present at 4 K, yet do not further degrade the photoluminescence efficiency above 4 K, the constant photoluminescence intensity up to 220 K provides strong evidence for pure radiative recombination over the full temperature window (see Methods). To be sure that the data for an individual wire are representative, we analysed more than 60 individual wires mechanically transferred from the high-crystal-quality sample I, which are presented in the right panels of Fig. 4b, c. The analysis shows that both the photoluminescence efficiency and the lifetime are almost temperature independent up to 300 K. If we attribute the small difference between the lifetimes at 4 K and 300 K to surface recombination, we obtain an upper bound to the surface recombination velocity of $S = 2.5 \times 10^4 \text{ cm s}^{-1}$, which is of similar magnitude³² as in cub-Ge nanowires, but still much larger than the lowest achievable³³ surface recombination velocity in Ge. We subsequently analyse the excitation power dependence of the emitted photoluminescence intensity in the inset to Fig. 4c. Importantly, the

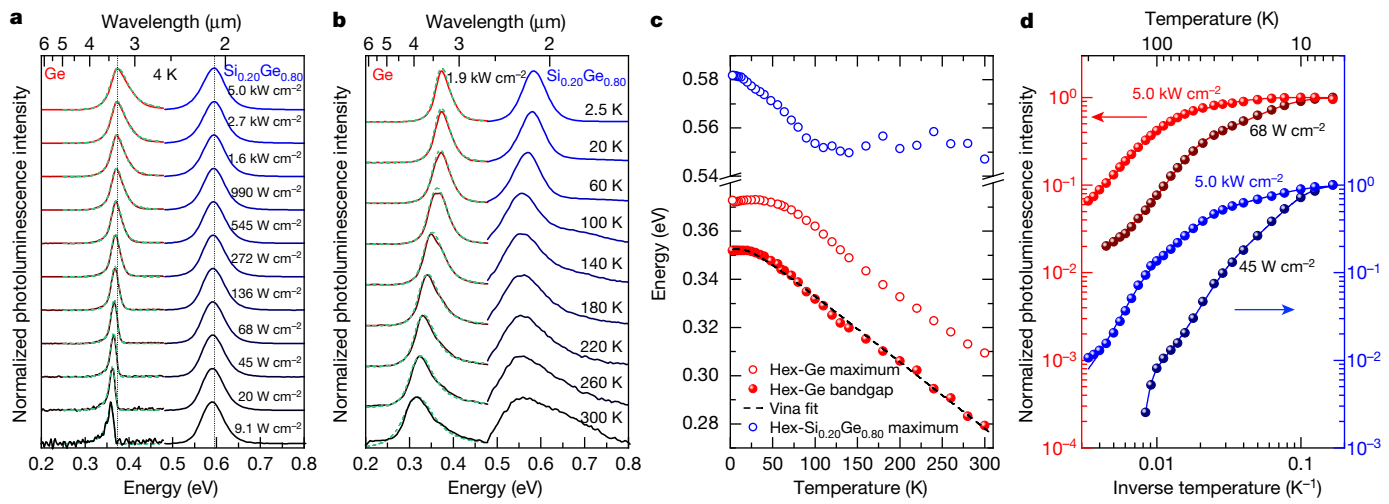


Fig. 3 | Emission from hex-Ge and hex-Si_{0.20}Ge_{0.80}. **a**, Excitation density-dependent photoluminescence spectra of hex-Ge (red to black) and hex-Si_{0.20}Ge_{0.80} (blue to black) measured on ensembles of as-grown nanowires, at 4 K. All spectra are normalized to their own maximum. The LSW fits of the Ge spectra are included as dashed lines, with the resulting fitting parameters in Extended Data Fig. 7a–c. Vertical dotted black lines highlight the shift and broadening of the peaks, indicating band-to-band emission. **b**, Temperature dependence of the photoluminescence spectra, normalized to their own maximum, measured at an excitation density of 1.9 kW cm⁻². A clear redshift and broadening are observed with increasing temperature, both indicating

band-to-band recombination. The fits with the LSW model are shown as dashed lines, with additional results in Extended Data Fig. 7d–f. **c**, Shrinkage of the bandgap with temperature, fitted using the Vina equation (see Methods). The open circles show the maxima of the photoluminescence as plotted in **b**, and the closed circles represent the bandgap determined by fits using the LSW model (see Methods). **d**, Arrhenius representation (see Methods) of the photoluminescence intensity as function of inverse temperature for hex-Ge (red) and hex-Si_{0.20}Ge_{0.80} (blue). All intensities are normalized to their respective intensity at 4 K. The reduced temperature dependence at higher excitation densities shows the approach towards the radiative limit.

plot shows a linear increase of the photoluminescence intensity with a slope very close to unity, which is consistent with a pure radiative decay mechanism (see Methods).

Because our measurements are performed in the radiative limit and the carriers accumulate in the direct minimum at low temperature, we

conclude that we observe direct-bandgap emission with a subnanosecond recombination lifetime. The combination of our theoretical predictions, structural microscopy data and luminescence data provides conclusive evidence for hex-Si_{1-x}Ge_x (0.65 < x < 1.00) being a new class of direct-bandgap semiconductors with a large optical matrix

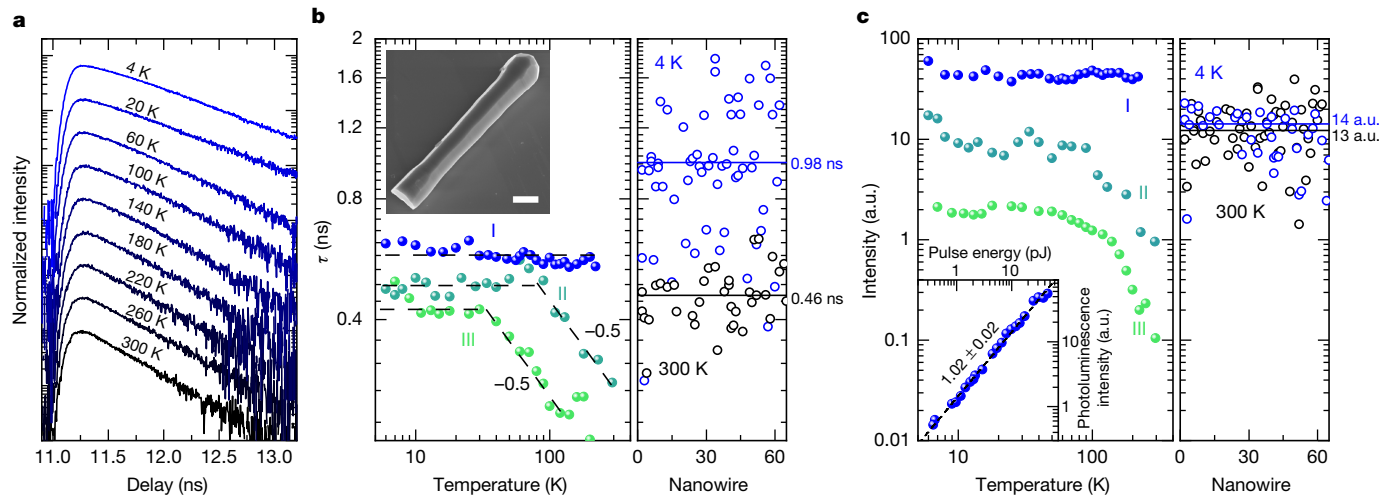


Fig. 4 | Time-resolved photoluminescence measurements of single hex-Si_{0.20}Ge_{0.80} nanowires. **a**, Photoluminescence lifetime measurements of hex-Si_{0.20}Ge_{0.80} recorded from a single wire for different temperatures from sample I (see sample details in Extended Data Fig. 8b). All decay traces show a single exponential decay and are vertically shifted for clarity. **b**, The left panel shows the temperature dependence of the lifetime for three hex-Si_{0.20}Ge_{0.80} wires, representing three different samples (I, II, III) with decreasing quality represented by blue to green colours. The onset of the reduction in lifetime due to non-radiative recombination shifts to higher temperature for higher quality wires, as emphasized by the dashed lines. The inset shows a representative scanning electron microscopy image of a single nanowire from sample I used for lifetime measurements. **c**, The right panel shows a comparison of the integrated photoluminescence intensity at 4 K and 300 K of the same wires measured in **b**, again showing a nearly temperature-independent radiative efficiency.

function of temperature for the same wires as in **b**, showing a nearly temperature-independent radiative efficiency for the best sample (I, blue). The photoluminescence intensities at 4 K scale approximately with the volume fractions of the samples (see Extended Data Fig. 8 for details). The inset shows the excitation power dependence of the integrated photoluminescence intensity, exhibiting a slope very close to unity. **b**, The right panel shows a comparison of the low-temperature (blue) and room-temperature (black) lifetime for a set of about 60 wires from sample I. The average lifetime shows a small decrease from 0.98 ns at 4 K to 0.46 ns at 300 K. **c**, The right panel shows a comparison of the integrated photoluminescence intensity at 4 K and 300 K of the same wires measured in **b**, again showing a nearly temperature-independent radiative efficiency.

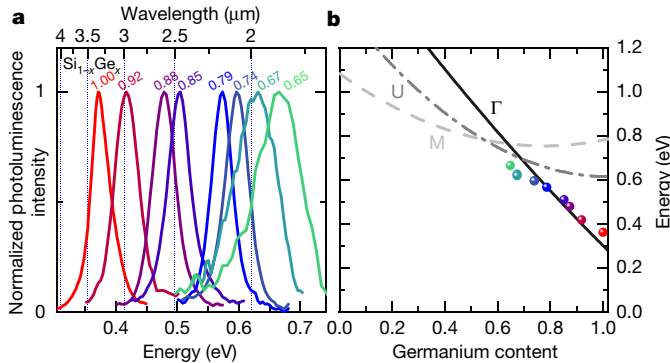


Fig. 5 | Tunability of the direct bandgap of hex-Si_{1-x}Ge_x alloys. **a**, Tunability of the photoluminescence spectra for different compositions. The spectra were recorded at 4 K at an excitation density of 1.9 kW cm⁻² on ensembles of as-grown samples. The spectra for hex-Si_{0.33}Ge_{0.67} and hex-Si_{0.35}Ge_{0.65} were measured on wires dispersed onto a silicon substrate capped with an Au layer (see Methods). **b**, Comparison of the measured peak energy as a function of the Ge content with the calculated emission band minima.

element. We subsequently compare the radiative transition rate of hex-SiGe with other direct-bandgap semiconductors. The radiative transition rate R_{rad} is quantified by $R_{\text{rad}} = B_{\text{rad}} \times n \times p$, where n and p are the electron and hole densities and B_{rad} is the coefficient for radiative recombination, which is directly related to the transition dipole moments. The coefficient B_{rad} can be deduced from a measurement of the pure radiative lifetime τ_{rad} using $B_{\text{rad}} = 1/(\tau_{\text{rad}} n_0)$, in which n_0 is the donor density. We obtain 0.7×10^{-10} cm³ s⁻¹ < B_{rad} < 8.3×10^{-10} cm³ s⁻¹ at 300 K, as explained in Methods, which is comparable in magnitude to GaAs³⁴ and InP³⁵ and almost five orders of magnitude larger³⁶ than for cub-Si (see Methods). Hex-Si_{1-x}Ge_x is thus in principle a fully Si-compatible semiconductor with a radiative emission strength comparable to a direct-bandgap group-III–V semiconductor.

Having established the direct nature of the bandgap of hex-Si_{1-x}Ge_x, we demonstrate how the size of the direct bandgap can be tuned via compositional engineering. Figure 5a shows photoluminescence measurements recorded at $T = 4$ K from the series of samples with $x = 0.65\text{--}1.00$. Bright emission is observed that redshifts with increasing Ge content from 0.67 eV ($x = 0.65$) to 0.35 eV ($x = 1.00$). The peak energy of the emission is compared in Fig. 5b with the calculated energy of the direct bandgap (at Γ) revealing excellent agreement. Clearly, the measured transition energies agree remarkably well with our theoretical predictions. The photoluminescence intensity versus composition indicates a direct-to-indirect crossover at $x = 0.65$ and efficient emission for hex-Ge as shown in Extended Data Fig. 9. The excellent agreement between theory and experiment provides not only a verification of the calculated bandgaps, but also provides strong support for the existence of a direct bandgap in hex-Si_{1-x}Ge_x for $x > 0.65$.

Direct-bandgap hex-Si_{1-x}Ge_x opens a pathway towards tight monolithic integration³⁷ of hex-Si_{1-x}Ge_x light sources with passive cub-Si photonics circuitry^{7–9} on the same chip. This will reduce stray capacitances, thereby increasing performance and reducing energy consumption, which is important for ‘green’ information and communication technologies. Now that the fundamental boundaries have been removed, a challenge is to get rid of the existing III–V substrate and the epitaxial template via the development of a hex-Si_{1-x}Ge_x technology platform that is fully compatible with complementary metal–oxide–semiconductor processes. Possible integration routes are strain-induced transformation²² of Si_{1-x}Ge_x, for instance by a dielectric (that is, SiO_x or SiN_x) strain envelope, or alternatively by template-assisted selective area growth of the hexagonal phase³⁸.

Online content

Any methods, additional references, Nature Research reporting summaries, source data, extended data, supplementary information, acknowledgements, peer review information; details of author contributions and competing interests; and statements of data and code availability are available at <https://doi.org/10.1038/s41586-020-2150-y>.

- Iyer, S. S. & Xie, Y. H. Light emission from silicon. *Science* **260**, 40–46 (1993).
- Miller, D. A. B. Silicon integrated circuits shine. *Nature* **384**, 307–308 (1996).
- Ball, P. Let there be light. *Nature* **409**, 974–976 (2001).
- Canham, L. Gaining light from silicon. *Nature* **408**, 411–412 (2000).
- Green, M. A., Zhao, J., Wang, A., Reece, P. J. & Gal, M. Efficient silicon light-emitting diodes. *Nature* **412**, 805–808 (2001).
- Vivien, L. Silicon chips lighten up. *Nature* **528**, 483–484 (2015).
- Atabaki, A. H. et al. Integrating photonics with silicon nanoelectronics for the next generation of systems on a chip. *Nature* **556**, 349–354 (2018).
- Wang, J. et al. Multidimensional quantum entanglement with large-scale integrated optics. *Science* **360**, 285–291 (2018).
- Cheben, P., Halir, R., Schmid, J. H., Atwater, H. A. & Smith, D. R. Subwavelength integrated photonics. *Nature* **560**, 565–572 (2018).
- Soref, R., Buca, D., Yu, S.-Q. & Group, I. V. Photonics: driving integrated optoelectronics. *Opt. Photonics News* **27**, 32–39 (2016).
- Raffy, C., Furthmüller, J., Bechstedt, F. Properties of hexagonal polytypes of group-IV elements from first-principles calculations. *Phys. Rev. B* **66**, 075201 (2002).
- De, A. & Pryor, C. E. Electronic structure and optical properties of Si, Ge and diamond in the lonsdaleite phase. *J. Phys. Condens. Matter* **26**, 045801 (2014).
- Cartoixa, X. et al. Optical emission in hexagonal SiGe nanowires. *Nano Lett.* **17**, 4753–4758 (2017).
- Rödl, C. et al. Accurate electronic and optical properties of hexagonal germanium for optoelectronic applications. *Phys. Rev. Mater.* **3**, 034602 (2019).
- Shen, Y. et al. Silicon photonics for extreme scale systems. *J. Lightwave Technol.* **37**, 245–259 (2019).
- Thomson, D. et al. Roadmap on silicon photonics. *J. Opt.* **18**, 073003 (2016).
- Muñoz, P. et al. Silicon nitride photonic integration platforms for visible, near-infrared and mid-infrared applications. *Sensors* **17**, 2088 (2017).
- Wang, R. et al. III–V-on-silicon photonic integrated circuits for spectroscopic sensing in the 2–4 μm wavelength range. *Sensors* **17**, 1788 (2017).
- Poulton, C. V. et al. Coherent solid-state LIDAR with silicon photonic optical phased arrays. *Opt. Lett.* **42**, 4091–4094 (2017).
- Soref, R. Enabling 2 μm communications. *Nat. Photon.* **9**, 358–359 (2015).
- Vincent, L. et al. Novel heterostructured Ge nanowires based on polytype transformation. *Nano Lett.* **14**, 4828–4836 (2014).
- Qiu, Y. et al. Epitaxial diamond-hexagonal silicon nano-ribbon growth on (001) silicon. *Sci. Rep.* **5**, 12692 (2015).
- Pandolfi, S. et al. Nature of hexagonal silicon forming via high-pressure synthesis: nanostructured hexagonal 4H polytype. *Nano Lett.* **18**, 5989–5995 (2018).
- He, Z., Maurice, J. L., Li, Q. & Pribat, D. Direct evidence of 2H hexagonal Si in Si nanowires. *Nanoscale* **11**, 4846–4853 (2019).
- Dushqai, G., Nayfeh, A. & Rasras, M. Hexagonal germanium formation at room temperature using controlled penetration depth nano-indentation. *Sci. Rep.* **9**, 15993 (2019).
- Hauge, H. I. T. et al. Hexagonal silicon realized. *Nano Lett.* **15**, 5855–5860 (2015).
- Hauge, H. I. T., Conesa-Boj, S., Verheijen, M. A., Kölling, S. & Bakkers, E. P. A. M. Single-crystalline hexagonal silicon-germanium. *Nano Lett.* **17**, 85–90 (2017).
- Würfel, P. The chemical potential of radiation. *J. Phys. C* **15**, 3967–3985 (1982).
- Lasher, G. & Stern, F. Spontaneous and stimulated recombination radiation in semiconductors. *Phys. Rev.* **133**, A553 (1964).
- Moss, T. S. The interpretation of the properties of indium antimonide. *Proc. Phys. Soc. B* **67**, 775–782 (1954).
- Wirths, S. et al. Lasing in direct-bandgap GeSn alloy grown on Si. *Nat. Photon.* **9**, 88–92 (2015).
- Prasankumar, R. P., Choi, S., Trugman, S. A., Picraux, S. T. & Taylor, A. J. Ultrafast electron and hole dynamics in germanium nanowires. *Nano Lett.* **8**, 1619–1624 (2008).
- Yablonovitch, E., Allara, D. L., Chang, C. C., Gmitter, T. & Bright, T. B. Unusually low surface-recombination velocity on silicon and germanium surfaces. *Phys. Rev. Lett.* **57**, 249–252 (1986).
- Lush, G. B. B-coefficient in n-type GaAs. *Sol. Energy Mater. Sol. Cells* **93**, 1225–1229 (2009).
- Semyonov, O., Subashiev, A., Chen, Z. & Luryi, S. Radiation efficiency of heavily doped bulk n-InP semiconductor. *J. Appl. Phys.* **108**, 013101 (2010).
- Trupke, T. et al. Temperature dependence of the radiative recombination coefficient of intrinsic crystalline silicon. *J. Appl. Phys.* **94**, 4930 (2003).
- Miller, D. A. B. Attojoule optoelectronics for low-energy information processing and communications. *J. Lightwave Technol.* **35**, 346–396 (2017).
- Staudinger, P., Mauthe, S., Moselund, K. E. & Schmid, H. Concurrent zinc-blende and wurtzite film formation by selection of confined growth planes. *Nano Lett.* **18**, 7856–7862 (2018).

Publisher's note Springer Nature remains neutral with regard to jurisdictional claims in published maps and institutional affiliations.

© The Author(s), under exclusive licence to Springer Nature Limited 2020

Article

Methods

Ab initio calculations

All calculations were performed using DFT as implemented in the Vienna Ab Initio Simulation Package (VASP)³⁹ with the projector augmented wave method. We used a plane-wave cutoff of 500 eV and we included Ge 3d electrons as valence electrons. Brillouin zone integrations were carried out using $12 \times 12 \times 6$ Γ-centred \mathbf{k} -point grids for lonsdaleite Ge and $12 \times 6 \times 6$ Γ-centred \mathbf{k} -point grids for Si-Ge, ensuring a convergence of total energies to 1 meV per atom. For structural calculations, the PBEsol exchange-correlation potential⁴⁰ was used, together with a convergence threshold of 1 meV Å⁻¹ on Hellmann–Feynman forces. The modified Becke–Johnson exchange potential in combination with the local density approximation (MBJLDA)⁴¹ was preferred for electronic structures and optical properties, as it guarantees bandgaps in excellent agreement with experiments⁴². We included spin–orbit coupling in all calculations. More details on the ab initio method and the selected approximations can be found in ref.¹⁴.

Alloys are studied using a cluster expansion method for isostructural lonsdaleite binary alloys⁴³. For the cluster expansion, the macroscopic alloy is divided into clusters of 8 atoms obtained from the primitive wurtzite unit cell. In this way, it is possible to study 46 different structures ranging from pure Ge to pure Si. This method becomes more accurate with increasing cluster size, and we verified that the thermodynamic averages are not appreciably modified by performing calculations with 16 atom clusters. The radiative lifetime τ_{rad} at temperature T is calculated using the formula:

$$1/\tau_{\text{rad}} = \sum_{cvk} A_{cvk} w_k f_{ck} (1 - f_{vk}) \quad (1)$$

where A_{cvk} denotes the radiative recombination rate for vertical optical transitions between a conduction state $|ck\rangle$ and a valence state $|vk\rangle$, with one-particle energies ε_{ck} and ε_{vk} , Fermi occupation functions f_{ck} and f_{vk} and the \mathbf{k} -point weight w_k . To reproduce the experimental conditions, we included $n_0 = 10^{19}$ cm⁻³ charge carriers attributable to n-doping in the conduction band, and modified the chemical potential of the electrons accordingly. The radiative recombination rate is given by:

$$A_{cvk} = n_{\text{eff}} \frac{e^2 (\varepsilon_{ck} - \varepsilon_{vk})}{\pi \varepsilon_0 \hbar^2 m^2 c^3 N_0} \frac{1}{3} \sum_{j=x,y,z} | \langle ck | p_j | vk \rangle |^2 \quad (2)$$

where n_{eff} is the refractive index of the effective medium (here set approximately to the experimental value for cub-Ge for which $n_{\text{eff}} = 5$) and N_0 denotes the number of charge carriers per unit cell. Denser \mathbf{k} -point grids were necessary to calculate the lifetimes ($72 \times 72 \times 36$ for lonsdaleite Ge and $24 \times 12 \times 12$ for Si-Ge).

Materials synthesis

The GaAs nanowires were grown in a close-coupled shower head metal organic vapour phase epitaxy (MOVPE) reactor via catalyst-assisted growth following the vapour–liquid–solid mechanism using Au catalyst seeds as schematically illustrated in Extended Data Fig. 1. The Au catalyst seeds were deposited in nanodisk arrays arranged on a GaAs (111)B substrate via the electron beam lithography technique. The growth was performed at a reactor flow of 8.2 standard litres per minute and a reactor pressure of 50 mbar. For the GaAs nanowires, the growth template was annealed at a set thermocouple temperature of 635 °C under an AsH₃ flow set to a molar fraction of $\chi_{\text{AsH}_3} = 6.1 \times 10^{-3}$. Then, the growth was performed at a set temperature of 650 °C with trimethylgallium (TMGa) and arsine (AsH₃) as material precursors set to molar fractions of $\chi_{\text{TMGa}} = 1.9 \times 10^{-5}$ and $\chi_{\text{AsH}_3} = 4.55 \times 10^{-5}$, respectively, resulting in a ratio of group V to III elements of 2.4. After the growth of the GaAs core nanowires, they are chemically treated with a

cyanide-based solution to remove the Au catalyst particles to avoid Au contamination in the SiGe shells. Eventually, the GaAs nanowire core is used as a hexagonal material template and was overgrown with a Si_{1-x}Ge_x shell by introducing suitable gas precursors for the shell growth, which are GeH₄ and Si₂H₆. The Si_{1-x}Ge_x shell was grown at a set temperature of 650–700 °C at a molar fraction of $\chi_{\text{SiGe}} = 1.55 \times 10^{-4}$ for various times until the desired thickness was reached.

Structural characterization

The structural quality of the crystals was investigated by TEM and XRD. For the TEM measurements, two different sample preparation methods were used. In the standard axial analysis, nanowires were mechanically transferred to a holey carbon TEM grid. For the cross-sectional TEM studies, nanowires were prepared using a focused ion beam. In both cases, high-resolution TEM and scanning TEM (STEM) analyses were conducted using a JEM ARM200F probe-corrected TEM operated at 200 kV. For the chemical analysis, EDX spectroscopy measurements were carried out using the same microscope equipped with a 100-mm² EDX silicon drift detector. TEM lamellae were prepared in a FEI Nova Nanolab 600i Dual Beam system. For this, the nanowires were initially transferred with the aid of a Kleindiek nano-manipulator from the growth substrate to a piece of Si and then arranged to lie parallel to each other. These nanowires were covered with electron- and ion-beam-induced metal deposition to protect them during the procedure. The lamella was cut out by milling with 30-kV Ga ions and thinned down with subsequent steps of 30-kV, 16-kV and 5-kV ion milling to minimize the Ga-induced damage in the regions imaged with TEM.

The XRD measurements were carried out at the Deutsches Elektronen Synchrotron (DESY) in Hamburg, at the high-resolution diffraction beamline P08. For the diffraction experiments a high-precision 6-circle diffractometer was used; the photon energy was set to 15 keV with a corresponding wavelength of 0.8266 Å. The energy was carefully chosen to ensure a high photon flux while still being able to access higher-indexed reflections, as needed for the precise measurements of the lattice parameters. The X-ray beam was shaped by a slit system and the resulting spot size on the sample was 200 μm (horizontal) × 100 μm (vertical), a size sufficient to illuminate a few thousand wires at once. For measuring the scattered signal coming from the wires, a Dectris Mythen one-dimensional X-ray detector was used; this detector offers a high dynamic range and, owing to the small pixel size (50 μm), an increased angular resolution in 2θ, compared to most two-dimensional detectors. For the conversion of the measured angular coordinates to reciprocal space coordinates and all further data processing, such as two-dimensional peak-fitting and post-processing for plotting, the freely available software library ‘Xrayutilities’ (<https://xrayutilities.sourceforge.io/>) in combination with Python 3.6 was used⁴⁴. The method used to determine the composition is given in Extended Data Fig. 3.

APT

For the APT measurements, individual nanowires were isolated from a forest of nanowires as described previously⁴⁵ with a Kleindiek nano-manipulator inside a FEI Nova Nanolab 600i Dual Beam. APT analyses were carried out in a LEAP 4000X-HR from Cameca. The system is equipped with a laser generating picosecond pulses at a wavelength of 355 nm. The experimental data were collected at laser or voltage pulse rates of 65–125 kHz with laser pulse energies of 5–10 pJ or pulse fractions of 25–27.5%. No substantial differences between laser and voltage pulses are seen, aside from a slightly higher compression of the core in the laser pulsed mode as discussed in ref.⁴⁶ and a lower quality of the mass spectra in the voltage pulsed mode. During the analysis the sample is kept at a base temperature of 20 K in a vacuum of about 2×10^{-11} mbar. Details of the APT measurement are explained in a previous publication⁴⁶.

Optical characterization

Time-correlated single-photon-counting measurements were performed on single $\text{Si}_{0.20}\text{Ge}_{0.80}$ wires. The wires were mechanically transferred onto a silicon wafer with a chromium (15 nm), Au (300 nm) and SiO_x (12 nm) top layer to act as a back mirror. This approach enhances the measured intensity and avoids potential optical signals emitted by the wafer.

The samples with transferred $\text{Si}_{0.20}\text{Ge}_{0.80}$ wires were mounted in an Oxford Instruments HiRes2 helium flow cryostat and were excited with a 1,030-nm, NKT ONEFIVE Origami femto-second pulsed laser with a 40-MHz repetition rate. The photoluminescence signal was measured in a backscattering geometry using a $36\times$ Au-coated Cassegrain objective, which focused the excitation laser to a spot of about 3 μm . The laser was filtered out of the photoluminescence signal using a 1,350-nm-long pass filter. Using an achromatic lens the photoluminescence signal was then focused onto a SM2000 single mode fibre and fed to a Single Quantum superconducting-nanowire single-photon detector that was optimized for >35% quantum efficiency at 1,800 nm and >15% quantum efficiency at 2,000 nm. The 1,350-nm-long pass filter in combination with the SM2000 fibre defined a spectral interval of 1,350 nm to about 2,300 nm over which photoluminescence was integrated. The time correlations between a laser pulse and a detection event were measured and counted using a PicoQuant PicoHarp 300 module. The overall instrumental response function shows a full-width at half-maximum (FWHM) of 96 ps with a decay time of $\tau_{\text{IRF}} = 21$ ps, which is the minimum observable decay time of the system. All measurements presented in Fig. 4 were performed with 125-pJ pulses resulting in an excitation density of about 0.4 mJ cm^{-2} per pulse, resulting in a much higher excitation density, and thus a stronger saturation of nonradiative processes than in Fig. 3d. The excitation energy was varied in the inset of Fig. 4c. All lifetime measurements were baseline corrected and fitted using a single exponential decay transient. The samples were found to be stable under our measurement conditions up to a fluence of 25 kW cm^{-2} .

Spectrally resolved photoluminescence experiments with accurate temperature control were carried out on as-grown samples mounted in an Oxford Instruments HiRes2 helium flow cryostat. The samples were illuminated using a 976-nm, continuous-wave laser, modulated at a frequency of 35 kHz, focused down to a 45- μm spot on the sample using a 2.1-cm focal distance off-axis parabolic Au mirror. The measurements presented in Fig. 3 (Fig. 5) were done on ensembles of approximately 400 (1,600) wires, deduced from a laser spot size of 45 μm and a pitch between the wires of 2 μm (1 μm). The same off-axis parabolic mirror was used to collimate the photoluminescence signal and couple it into a Thermo Scientific Nicolet iSS50r Fourier-transform infrared spectrometer (FTIR), equipped with an HgCdTe detector, used for $\text{Si}_{1-x}\text{Ge}_x$ samples with $x > 0.80$ and an extended InGaAs detector, used for samples with $x \leq 0.80$. The FTIR was operated in step-scan mode, which allowed us to use a lock-in technique to substantially increase sensitivity and to eliminate the thermal background. To minimize parasitic absorption, the full optical path was purged with nitrogen.

XRD RSMs

For all measured samples at least three individual hexagonal reflections were measured. For the pure hex-Ge sample, the azimuth was varied to enhance the fidelity of the extracted lattice parameters. In addition, a cub-GaAs substrate reflection was always used as an anchor in reciprocal space to correct for any possible alignment offsets. From the measured symmetric reflections (see the full series in Extended Data Fig. 4), one could calculate and correct for the tilt of the lattice planes ($[111]$, $[0001]$) with respect to the sample's surface. Furthermore, the $Q_{\text{out-of-plane}}$ position of the wurtzite (0008) reflection allows us to calculate the lattice parameter c , corresponding to the $[0001]$ crystal direction. For some Ge concentration the (0008) nanowire reflection coincides with the cubic (444) substrate reflection, which makes a

systematic evaluation of the symmetric RSMs complicated, so we also measured asymmetric space maps, around reflections that are only allowed in the hexagonal crystal lattice. The position of the asymmetric reflections in reciprocal space allows us to extract the in- as well as out-of-plane lattice parameters a and c . In Fig. 2e a series of hex-($\bar{1}018$) reflections for all measured Ge-concentrations is shown. The peak position sensitively depends notably on the amount of Ge present in the alloy, and lower Ge concentrations result in lower lattice parameters a and c , which are closer to the native lattice parameters of hex-Si²⁶. For all RSMs shown, the $Q_{\text{out-of-plane}}$ direction corresponds to the crystalline $[0001]$ direction, and the $Q_{\text{in-plane}}$ direction corresponds to the $[\bar{1}010]$ direction, both in the hexagonal system, indicated by the four Miller–Bravais indices.

We estimated the stacking-fault density to be around 2–4 stacking faults per micrometre by calculating the average peak widths along the $[0001]$ direction of the wurtzite reflections shown in Fig. 2e. Owing to the presence of stacking faults, the coherently diffracting domains along a given crystalline direction have only a finite size. The limited size of these domains leads to crystal-size effects when performing XRD measurements. The broadening of the diffraction peaks along a certain direction scales inversely proportionally with the average size of a defect-free domain along the same direction, which is a measure of the average distance between defects. Narrow peaks indicate the presence of long defect-free segments or domains in the nanowires. To further confirm the high crystal quality of the samples, an asymmetric crystal-truncation-rod scan in combination with a polar scan for $\text{Si}_{0.20}\text{Ge}_{0.80}$ composition is shown in Extended Data Fig. 5. Since this approximation does not consider other effects that can lead to a peak-broadening (such as micro-strains in the presence of defects) we treated the given, calculated value as an estimate. TEM measurements on the same set of samples, however, show very consistent defect densities, confirming the low number of stacking faults.

To accurately determine the peak positions, all RSMs were corrected according to the peak positions of the cub-GaAs substrate reflections to eliminate any angular alignment offsets. Then a two-dimensional Gaussian fit was performed on the datasets in q -space before gridding, to reduce the influence of possible artefacts coming from the gridding routine. For plotting the dataset, the irregularly spaced q -coordinates, as measured and transformed from the angular-space, were gridded into a regularly spaced q -coordinate system.

The combined results from the XRD measurements can be found in Extended Data Fig. 4g, where the measured lattice parameters are given for each measured Ge concentration. For all samples the influence of the wurtzite-GaAs core material on the $\text{Si}_{1-x}\text{Ge}_x$ lattice parameter can be neglected, because the relatively thin GaAs core (around 35 nm) is surrounded by a thick (several 100 nm) $\text{Si}_{1-x}\text{Ge}_x$ shell. Hence, the crystalline properties of the hex- $\text{Si}_{1-x}\text{Ge}_x$ shell dominate the whole structure. Furthermore, hex-Ge and wurtzite-GaAs are nearly lattice matched (see lattice parameter of wurtzite-GaAs⁴⁷), which implies that basically no strain in the shell is expected for the samples with high Ge concentrations ($x > 0.60$), as also confirmed by the finite element method simulation. This is important because it confirms the high fidelity of the lattice parameters found, especially for the lattice parameter of pure hex-Ge. The errors given in Extended Data Fig. 4g represent the accuracy of defining the peak position with a two-dimensional fit as described, as well as the scattering of the individual lattice parameter values extracted from the evaluation of multiple peaks. The instrumental resolution can be neglected for the error estimation, since the contribution to the given errors will be much smaller than the total error values.

The LSW model

The observed photoluminescence spectra of hex-Ge and hex-SiGe all consist of a single peak. We attribute the observation of a single photoluminescence peak to a band-to-band recombination. The absence

Article

of excitonic effects at low temperatures is due to an As-doping level of $9 \times 10^{18} \text{ cm}^{-3}$ as deduced by APT (shown in Extended Data Fig. 6). At this doping level, individual As dopants, which are expected to be shallow in a small-bandgap semiconductor, will merge into a doping band, which in turn is expected to merge⁴⁸ with the conduction band. GaAs nanowires with a similar doping level⁴⁹ also show single-peak photoluminescence spectra that are very similar to our findings for hex-SiGe. To accurately establish whether the observed photoluminescence is due to band-to-band recombination, we fitted the experimental spectra with the LSW model^{28,29,49,50}.

Description of the LSW model. The LSW model, which predicts the shape of a band-to-band photoluminescence peak, is derived from the Planck–Einstein radiation law⁵¹ and is given by equation (3).

$$I_{\text{PL}} = \frac{2\pi}{h^3 c^2} \frac{E^2 a(E)}{\exp\left(\frac{E-\Delta\mu}{k_B T}\right) - 1} \quad (3)$$

where k_B is Boltzmann's constant. The LSW model depends only on $\Delta\mu$ (which is the splitting of the electron and hole quasi-Fermi levels), the electron temperature T and the absorptivity $a(E)$. The absorptivity is dependent on the absorption coefficient $\alpha(E)$ as follows: $a(E) = [1 - \exp(-\alpha(E)d)]$, in which d is a characteristic length scale over which light is absorbed. To use this model a description of the absorption coefficient is made in which parabolic bands are assumed. This implies that the joint density of states (JDOS) scales as the square root of energy as follows: $\text{JDOS} \propto \sqrt{E - E_g}$, in which E_g is the bandgap energy. With the additional assumption that the transition matrix element is k -independent, we can state that the absorption coefficient scales proportionally to the JDOS and is given by $\alpha_0(E) = C \sqrt{E - E_g}$ where C is a fitting parameter into which the characteristic length scale d is absorbed. Additionally, an Urbach tail is taken into account by convoluting $\alpha_0(E)$ with a peak function $T(E, \gamma)$ given by: $T(E, \gamma) = N \exp\left(-\left|\frac{E - E_g}{\gamma}\right|\right)$

in complete analogy with ref.⁵⁰, where γ is a characteristic width of the function and N is a normalization constant that ensures that the integral of the peak remains unity. Lastly, the absorption coefficient is strongly dependent on the level of excitation and needs to be corrected for this (that is, already excited states can no longer contribute to absorption). To do so, the filling of the valence and conduction band needs to be taken into account, leading to an additional correction factor $(f_v(E, \mu_h) - f_c(E, \mu_e))$, which is the Fermi–Dirac distribution of the holes minus the Fermi–Dirac distribution of the electrons, which are dependent on their respective quasi-Fermi levels μ_h and μ_e . To make this correction term compatible with the full model, the Fermi–Dirac distributions must be expressed in terms of $\Delta\mu = \mu_e - \mu_h$, which requires additional assumptions. This problem is addressed for two different cases. For the case of high excitation (when the excitation-induced carriers are dominating over the doping-induced carriers) the quasi-Fermi levels are symmetrically split around the intrinsic Fermi level⁵⁰, leading to equation (4):

$$(f_v(E, \mu_h, T) - f_c(E, \mu_e, T)) = f(E, \Delta\mu, T) = 1 - \frac{2}{\exp\left(\frac{E-\Delta\mu}{2k_B T}\right) + 1} \quad (4)$$

This, however, is a reasonable assumption only when the effective masses of the conduction and valence band are similar. The other case to be considered is the low-excitation regime, where free carriers due to doping are dominant over excited carriers. On account of degenerate n-type doping, μ_e will be determined only by the doping concentration and is independent of the excitation density. On the other hand, μ_h will be determined by the number of minority carriers and is therefore dependent on the excitation density. Nonetheless, at low temperatures it can be assumed that μ_h will lie very close to the valence band edge

because of the step-like nature of the Fermi–Dirac distribution. This allows us to assume that $\mu_h = 0$ and that $\mu_e = \Delta\mu$, where zero energy is chosen at the valence band maximum. This low-excitation regime therefore results in a correction term, given in equation (5):

$$(f_v(E, \mu_h, T) - f_c(E, \mu_e, T)) = f(E, \Delta\mu, T) = \frac{1}{2} - \frac{1}{\exp\left(\frac{E-\Delta\mu}{k_B T}\right) + 1} \quad (5)$$

In our fitting, we have made use of both cases, but we note that the apparent difference between the two cases is negligible at high excitation densities. Adding all these ingredients together, a full model for the absorptivity is given by equation (6) and the LSW model can be utilized:

$$\begin{aligned} & a(E, E_g, \Delta\mu, T, \gamma, C) \\ &= 1 - \exp\{-[\alpha_0(E, E_g, C) * T(E, \gamma)](f_v - f_c)(E, \Delta\mu, T)\} \end{aligned} \quad (6)$$

Fitting results. Shifting our attention back to Fig. 3a, b, the high-quality fits using the LSW model unambiguously show that the observed photoluminescence is exclusively due to band-to-band recombination over the full excitation density and temperature range. It is of paramount importance for the analysis performed that measured recombination lifetimes are due to band-to-band recombination and not due to an impurity or defect-related optical transition, for example.

Additional fitting results of the power series presented in Fig. 3a are shown in Extended Data Fig. 7a–c. The quasi-Fermi-level splitting $\Delta\mu$ and the bandgap are plotted in Extended Data Fig. 7a, the electron temperature is plotted in Extended Data Fig. 7b and the broadening parameter γ is plotted in Extended Data Fig. 7c as a function of the excitation density. Fits were performed with the low-excitation-case as discussed above, to get the best result on the low-excitation side of the series. An encouraging result is the constant bandgap as a function of excitation density up to around 2 kW cm^{-2} , which provides great trust in the accuracy of the model. The shrinkage of the bandgap thereafter suggests the onset of bandgap renormalization (that is, the excitation-induced minority carrier density is starting to be of the order of the majority carrier density). The quasi-Fermi-level splitting $\Delta\mu$ is increasing over the full excitation range, which seems to contradict the previous assumption that both μ_h and μ_e are independent of the excitation density at low excitation. The argument for the Fermi level of the minority carriers (in our case μ_h), however, considers a hard onset of the density of states, yet a clear broadening of this onset is observed of at least 15 meV, as shown by the values we determined for the broadening parameter γ (Extended Data Fig. 7c). This means that, despite the low lattice temperature, at low pump powers only μ_e is independent of the excitation density and μ_h is still positioned within the bandgap. This suggests that only the tail of the density of states is populated with holes. As a consequence, the quasi-Fermi-level μ_h is still expected to shift down with increasing excitation density, which might provide an explanation for the observation of an increasing quasi-Fermi-level splitting in Extended Data Fig. 7a. At low excitation, a temperature as low as 32 K is observed, but above an excitation density of about 300 W cm^{-2} , the carrier temperature starts to rise substantially. Even though thermal equilibrium should be established between the lattice and the charge carriers²⁸, this is not a necessary assumption for the model as long as the electrons and holes are in mutual thermal equilibrium. The electron temperature (and therefore also the hole temperature) can thus be much higher than the lattice temperature. Group-IV materials are nonpolar and are thus lacking dipole active optical phonons. Owing to the absence of the long-range Fröhlich interaction^{52–54}, the observation of a hot carrier distribution is not surprising.

For the temperature-dependent data shown in Fig. 3b, additional results are shown in Extended Data Fig. 7d–f. The data obtained from the LSW analyses for the bandgap and the quasi-Fermi-level splitting

are shown in Extended Data Fig. 7d, the fitted electron temperature is shown in Extended Data Fig. 7e and the broadening parameter γ is shown in Extended Data Fig. 7f. It has already been shown in Fig. 3c that the bandgap as function of temperature fits very well to the expected Vina equation, as further discussed in the Methods section ‘Temperature dependence of the fundamental bandgap’. The marginal underestimation of the bandgap by the LSW fit in the temperature range 70 K to 150 K is probably due to a faint absorption line at 0.363 eV, which is also visible in the photoluminescence spectra depicted in Fig. 3a. The value for $\Delta\mu$ increases by 24 meV with respect to the bandgap for a temperature increase from 2.5 K to 70 K. This behaviour happens in combination with an increase in the γ -parameter of 3.5 meV, as depicted in Extended Data Fig. 7f, which suggests that deep donors are being ionized. This effect is further supported by the decrease in electron temperature shown in Extended Data Fig. 7e for the same lattice-temperature interval of 2.5 K to 70 K, because, owing to carrier–carrier scattering, photo-excited carriers are expected to cool faster when the density of majority carriers is increased. At temperatures above 70 K, $\Delta\mu$ does not further increase with respect to the bandgap within a 10-meV margin, indicating that all (deep) dopants are fully ionized at temperatures above 70 K. The electron temperature increases with a much steeper slope than the lattice temperature for lattice temperatures above 70 K, which is due to the high excitation density for this series.

Determination of the electron quasi-Fermi level and the doping density

The APT measurements as presented in Extended Data Fig. 6 yield the total incorporated atomic concentrations of dopant atoms. We are, however, more interested in the activated donor density, which can be obtained from the LSW model. This model yields the electron-Fermi level, which allows us to calculate the corresponding activated electron density. As discussed, based on Extended Data Fig. 7d, for lattice-temperatures higher than 70 K all (observable) dopants are ionized and have donated their charge-carriers to their respective bands. If the photoluminescence is probed in the low-excitation regime, the total Fermi-level splitting $\Delta\mu$ can be assumed to be equal to the electron-Fermi level μ_e . However, for the photoluminescence temperature series presented in Fig. 3b and Extended Data Fig. 7, the electron temperature is significantly above the lattice temperature, which can give rise to an additional splitting of the Fermi levels not induced by the doping. Thus, to find a reasonable value for $\Delta\mu = \mu_e$, we choose to perform a LSW fit (see Extended Data Fig. 7g) on a photoluminescence measurement at 80 K such that all donors are ionized and at a reduced excitation density of 45 W cm⁻² (compared to 1.8 kW cm⁻² in Extended Data Fig. 7e), ensuring that $\Delta\mu$ is only influenced by the doping and not by the electron temperature. The result of the LSW model is an electron temperature of 88 K, indicating that the measurement is indeed in the low-excitation regime. In addition, we obtain a value μ_e of 32 meV for the electron-quasi-Fermi level with respect to the conduction-band minimum and a broadening parameter γ of 27 meV. To find the doping density associated with this Fermi level the density of states for parabolic bands is assumed to be given by⁵⁵ equation (7):

$$\text{DOS}_{\text{cb}}(E) = \frac{1}{2\pi^2} \left(\frac{2m_{\text{eff,C}}}{\hbar^2} \right)^{\frac{3}{2}} \sqrt{E - E_g} \quad (7)$$

Here, $m_{\text{eff,C}}$ is the averaged effective mass of the conduction band using equation (8)⁵⁶ to average over the different \mathbf{k} -directions. Using the values found from DFT calculations¹⁴ for hex-Ge we find an effective mass of 0.20.

$$m_{\text{eff,C}} = (m_{\Gamma-K} m_{\Gamma-A} m_{\Gamma-M})^{\frac{1}{3}} \quad (8)$$

To find the doping concentration, equation (7) should be multiplied with the electron Fermi–Dirac equation and integrated, resulting in equation (9).

$$n_0 = \int_0^\infty \text{DOS}_{\text{cb}}(E) f(T, \mu_e) dE \quad (9)$$

We evaluated the integration of equation (9) numerically, taking into account an Urbach tail with a broadening parameter γ of 27 meV and using the actual Fermi–Dirac distribution. This results in a doping density of $n_0 = 3 \times 10^{18} \text{ cm}^{-3}$. We note, however, that this value should be considered a lower boundary because of the limitations of the parabolic-band approximation.

Temperature dependence of the fundamental bandgap

Although the temperature dependence of the fundamental bandgap is most often described by the Varshni equation⁵⁷, the Vina equation⁵⁸ provides a more accurate description at elevated temperatures:

$$E_g = a - b \left(1 + \frac{2}{\exp\left(\frac{\theta}{T}\right) - 1} \right) \quad (10)$$

in which a is a constant, b represents the strength of the electron–phonon interaction, and θ is the Debye temperature of the material. To analyse the temperature dependence of the bandgap of hex-Ge, the Vina equation is fitted to Fig. 3c, where the following values are found: $a = 0.36 \text{ eV}$, $b = 9.2 \text{ meV}$ and a Debye temperature of $\theta = 66 \text{ K}$.

The shrinkage of the Si_{0.20}Ge_{0.80} bandgap, which is displayed in Fig. 3c, follows a different behaviour owing to the compositional fluctuations⁵⁹ of the crystal. The initial fast shift of the apparent bandgap is probably due to the carrier thermalization towards compositional pockets with lower bandgap, while the apparent deviation from the Vina law at high temperature is most probably because the spectrum should be interpreted as a convolution of the Fermi–Dirac distribution with a Gaussian broadening function caused by the compositional fluctuations, the details of which are beyond the scope of the present paper.

Temperature dependence of the photoluminescence intensity

Here we provide a detailed Arrhenius analysis of the temperature dependence of the integrated photoluminescence as presented in Fig. 4c. Our goal is to provide quantitative information about the ratio between the radiative and non-radiative recombination rates. To explain the temperature dependence of the photoluminescence emission intensity, we first have to set up the proper rate equation model. Since the donors have merged into a donor band that shifted into the conduction band, we will not incorporate the donor level into the rate equation model. Following the LSW analysis, we concluded that the photoluminescence spectrum can be explained by band-to-band recombination with only a minor influence of the acceptor-related transition. As a consequence, we limit our rate equation model to a three-level system incorporating the conduction band, the valence band and a ‘killer defect’, which is characterized by an activated non-radiative recombination lifetime. We thus use the one-centre model in the classification of Reschchikov⁶⁰, which is explained in more detail by a configuration coordinate diagram. In this one-centre model, the internal quantum efficiency η_{int} for radiative emission varies with temperature according to the ratio of the radiative recombination rate, divided by the total recombination rate: $\eta_{\text{int}} = \tau_r^{-1}/(\tau_r^{-1} + \tau_{\text{nr}}^{-1}(T))$. The low excitation data collected at 68 W cm⁻², which are presented in Fig. 3d, can be fitted with this formula by assuming that the non-radiative recombination rate is thermally activated with activation energy E_a by $\tau_{\text{nr}}^{-1}(T) = \tau_{\text{nr},0}^{-1} e^{-E_a/k_B T}$, similar to group III–V materials^{61–65}.

Article

The excellent quality of the Arrhenius fit provides evidence that the non-radiative recombination into the yet-unknown killer defect can indeed be explained by an activated non-radiative recombination rate.

The temperature dependence of the photoluminescence intensity can thus be expressed as:

$$I(T) = \frac{I_0}{1 + R_A e^{\frac{-E_a}{k_B T}}} \quad (11)$$

which the photoluminescence quenching rate^{61–65} into the non-radiative centre A is given by $R_A = \frac{\tau_r}{\tau_{nr,A,0}}$. In most semiconductors, different non-radiative recombination centres A and B exist, which feature activation energies $E_{a,A}$ and $E_{a,B}$ and quenching rates R_A and R_B , resulting in:

$$I(T) = \frac{I_0}{1 + R_A e^{\frac{-E_{a,A}}{k_B T}} + R_B e^{\frac{-E_{a,B}}{k_B T}}} \quad (12)$$

It is instructive to perform this analysis on three different generations of hex-SiGe samples, which are specified in Extended Data Fig. 8b and whose Arrhenius plots are shown in Extended Data Fig. 8a. In sample III, we observe a first quenching mechanism with activation energy $E_A = 16 \pm 1$ meV with a quenching efficiency of $R_A = 3 \pm 1$, and a second quenching mechanism with $E_B = 91 \pm 2$ meV and $R_B = 6 \times 10^2 \pm 1$, which is at least partially due to surface recombination. These rates imply an internal quantum efficiency of $\frac{\tau_r^{-1}}{\tau_r^{-1} + \tau_{nr,A,0}^{-1} + \tau_{nr,B,0}^{-1}} = 0.15\%$ when both non-radiative channels are fully activated (room temperature). The first quenching mechanism seems to have disappeared in sample II, which was grown at a higher temperature. In sample II, we observe photoluminescence quenching only above a temperature of 100 K, which is again tentatively attributed to be at least partially due to surface recombination. The activation energy $E_B = 34 \pm 5$ meV is tentatively explained by the de-trapping from localized states due to alloy fluctuations in the hex-SiGe nanowire shell. Once the carriers are de-trapped, they will quickly diffuse towards the nanowire surface where they recombine non-radiatively. In sample I, both quenching mechanisms have disappeared as $R_A = \frac{\tau_r}{\tau_{nr,A,0}} = 0$ and $R_B = \frac{\tau_r}{\tau_{nr,B,0}} = 0$ at an excitation density of about 0.4 mJ cm⁻² per pulse, thus showing that sample I remains in the radiative limit up to 220 K. The quality of sample I is probably higher owing to its thick hex-SiGe shell, which reduces the amount of surface recombination, and to its length, which reduces the influence of re-evaporating arsenic (As) and gallium (Ga) from unwanted growth on the substrate. To be completely sure, we regrew sample I, resulting in a temperature dependence identical to that of the first grown sample.

Comparison with group III–V semiconductors

The measured lifetime of hex-Si_{0.20}Ge_{0.80} at low temperature is very comparable to the reported recombination lifetimes^{66–68} in literature for III–V compound semiconductors, which are generally of the order of 1 ns. Jiang et al.⁶⁹ reported a temperature-independent lifetime of 1 ns in core/shell GaAs/AlGaAs nanowires, very similar to our as-yet unpassivated hex-Si_{0.20}Ge_{0.80} nanowire shells. The quenching ratio of the integrated photoluminescence intensity when increasing the temperature from 4 K to 300 K compares quite favourably to that of hex-SiGe, where this ratio varies around a factor of 15–100 as shown in Fig. 3d. Ref. ⁶⁵ found a photoluminescence quenching ratio of the order of 10⁵ for InGaP. Ref. ⁶³ observed a quenching ratio around 200 for GaAsSb/GaAs quantum wells. Ref. ⁶¹ also observed quenching ratios above 100 for undoped GaN and 1,000 for Mg-doped GaN. The photoluminescence quenching in Ge microstrips as obtained by ref. ⁷⁰ is comparable to ours.

Temperature dependence of the radiative lifetime

As shown in Fig. 4b, we observe a temperature-independent recombination lifetime in sample I. Here we show that such a

temperature-independent recombination lifetime can only be explained by radiative recombination in a degenerately doped semiconductor.

Non-radiative recombination features an activated behaviour at low temperature, which is governed by $\tau_{nr}^{-1}(T) = \tau_{nr,0}^{-1} e^{-E_a/k_B T}$ as explained in the Methods section ‘Temperature dependence of the photoluminescence intensity’. By analysing the well known expressions for the Shockley–Read–Hall (SRH) non-radiative recombination mechanism for intrinsic material, the SRH lifetime can be expressed^{31,71} as $\tau_{SRH} = \tau_{p,0} \left(1 + \cosh \frac{E_t - E_i}{k_B T} \right)$ in which E_t is the trapping level, E_i is the intrinsic Fermi level and $\tau_{p,0}$ is the SRH lifetime for minority holes. At higher temperature, the SRH lifetime is expected to decrease with $T^{-1/2}$ owing to the fact that both $\tau_{r,0}$ and $\tau_{p,0}$ are inversely proportional to the thermal velocity. We conclude that it is not possible to interpret the observed temperature independent recombination lifetimes as being due to non-radiative recombination.

We next discuss the possibility that surface recombination is already partially masking radiative recombination at 4 K. We believe that in hex-SiGe, the carriers are most likely to be localized at 4 K owing to alloy fluctuations within the nanowires, and are not capable of reaching the surface. We actually attribute the decrease of the photoluminescence intensity and lifetime in sample III (thinnest shell, highest surface recombination loss; see Extended Data Fig. 8b) to surface recombination with a measured activation energy of 91 meV (Extended Data Fig. 8a). Extended Data Fig. 8 also shows that the photoluminescence intensity at 4 K is quite accurately proportional to the material volume, which is another compelling argument to exclude the strong influence of surface recombination at 4 K.

Next, we discuss Auger recombination, which might be expected from the high n-doping by unintentional arsenic (As) incorporation during growth. The Auger rate includes two different processes^{72,73}, the nnp-Auger process, in which the excess energy is transferred to an electron, and the npp-Auger process, in which the excess energy is transferred to a hole. In our case, we have high n-doping due to As incorporation during growth, resulting in a doping concentration of n_0 . We expect that the nnp-Auger process will be most important in our n-doped hex-SiGe samples. The Auger coefficients are, however, temperature-dependent⁷⁴, which results in a temperature-dependent recombination lifetime, which is not consistent with our observations. Most importantly, as shown in the inset of Fig. 4c, we observe a linear relation between the integrated photoluminescence intensity and the excitation power. We do not observe a decrease of the photoluminescence intensity at high excitation, which is a strong indication that Auger processes are still weak at our experimental conditions.

We are thus left with radiative recombination. The radiative lifetime for an intrinsic semiconductor increases⁷⁵ with $T^{3/2}$ showing subnanosecond radiative lifetimes at low temperature, which increase to more than a microsecond at room temperature. For a degenerately doped semiconductor, the radiative lifetime is expected to be temperature independent since the B-coefficient for radiative recombination is proportional to L/np , in which L is the spontaneous radiative recombination rate²⁹. It can be easily seen that for a degenerate semiconductor $p \propto T^{3/2}$, $L \propto T^{3/2}$, while n becomes temperature independent. Both the B-coefficient for radiative recombination rate and the radiative lifetime are thus expected to be independent of temperature.

We present the photoluminescence lifetime measurements for all three samples in Fig. 4b. We recall our conclusion from Fig. 4c that samples III, II and I are in the radiative limit up to 40 K, 100 K and >220 K, respectively. This behaviour is exactly reproduced in Fig. 4b, in which the lifetimes are constant up to 40 K, 90 K and >220 K, respectively. For samples III and II, non-radiative recombination becomes the dominant recombination mechanism above 40 K and 90 K, respectively, as is clear from the observed slope, which is close to –0.50, as expected for non-radiative SRH recombination at high temperature. The non-radiative

recombination at high temperature is expected to be due to recombination at the nanowire surface.

To obtain statistics, we performed photoluminescence lifetime measurements on more than 60 different nanowires taken from sample I at 4 K and at 300 K. The data are displayed in the right panels of Fig. 4b, c. We observe a spread in the recombination lifetimes at 4 K, which we attribute to variations of the local density of photonic states around each individual wire. The nanowires have ‘wavelength-scale’ dimensions in the radial direction and their length of 2.5–8 μm would be expected to result in a small number of longitudinal optical modes being resonant with the peak of the gain spectrum in the hex-SiGe gain material. As discussed previously for group-III–V nanowire lasers, these aspects give rise to high spontaneous emission coupling efficiencies (large β -factors) for emission into longitudinal modes of the nanowire and strong modifications of the rate and directionality of radiative recombination⁷⁶. The microscopic reason for this can be traced to the back action of the reflected field at the dielectric–vacuum interface on the local emitted field by the emitter^{77,78}. Equivalently, the effect can be described as the variation in the local density of optical states (LDOS), or a position-dependent spontaneous emission rate of the nanowire. Such effects in our nanowires would be expected to translate to a weakly oscillatory ‘length-dependent’ variation of the radiative emission rate and our observations of wire-to-wire lifetime variations are entirely consistent with this picture.

Excitation power dependence of the integrated photoluminescence intensity

At low excitation density, $\Delta n < n_0$, and the nonradiative, radiative and Auger processes all yield a linear dependence of the photoluminescence-intensity versus excitation power with a slope of unity, which suggest that we cannot draw any conclusions from the data in this range of excitation power. However, this simplified analysis assumes that the non-radiative recombination centres are not being saturated.

Since we do not observe any deviation from a linear behaviour, our data suggest that, even if non-radiative recombination centre were present, we are unable to saturate them with excitation power. This suggests that we do not have any non-radiative recombination centres in the bulk of the material, implying that we are already in the radiative limit. We note that this argument applies both for $\Delta n < n_0$ and $\Delta n > n_0$.

At high excitation density, $\Delta n > n_0$, we will use the analysis of Yoo et al.⁷⁹. In their analysis, the total carrier generation rate G should be equal to the total carrier recombination rate by:

$$G = An + Bn^2 + Cn^3 \quad (13)$$

in which An is the SRH nonradiative recombination rate, Bn^2 is the radiative recombination rate and Cn^3 is the Auger nonradiative rate. At high excitation density (which is above 500 W cm^{-2} for hex-Ge as shown by bandfilling in Fig. 3a) when the photo-injected carrier densities Δn , Δp are larger than the electron concentration due to unintentional As-doping (see APT measurements in Extended Data Fig. 6), we expect the behaviour predicted by ref. ⁴⁴.

$$G = A\sqrt{\frac{I_{\text{PL}}}{aB}} + \frac{I_{\text{PL}}}{a} + C\left(\frac{I_{\text{PL}}}{aB}\right)^{3/2} \quad (14)$$

In the plot of the integrated photoluminescence intensity versus excitation density⁸⁰, equation (14) yields a slope of two for non-radiative recombination (provided that the non-radiative recombination centres are not being saturated; see above), a slope of unity for radiative recombination and a slope of 2/3 for Auger recombination. We note that we do not observe a decrease of the photoluminescence intensity at the highest excitation power, providing a first indication that Auger recombination losses are not yet dominant in this material.

For the hex-Si_{0.20}Ge_{0.80} sample, we are not yet able to establish a clear boundary between the $\Delta n < n_0$ and the $\Delta n > n_0$ regimes owing to the added complication of alloy broadening. Most probably, the Si_{0.20}Ge_{0.80} alloy will be composed of compositional pockets in which either $\Delta n < n_0$ or $\Delta n > n_0$ applies. The observation of a slope of exactly unity, as shown in the inset of Fig. 4c, implies that both types of pocket are in the radiative limit.

B-coefficient of hex-SiGe

To compare the radiative emission strength of hex-SiGe with other well known direct-bandgap semiconductors such as GaAs or InP, we compare the radiative emission rate at room temperature, which is most relevant for device applications. By making the comparison at 300 K, excitonic effects as well as effects due to carrier localization in the hex-SiGe alloy are no longer relevant. The key parameter to compare the radiative efficiency of a semiconductor is the *B*-coefficient, which is a recombination rate, corrected for the doping density.

The radiative rate per volume of a semiconductor R_{rad} can be expressed in terms of the *B*-coefficient, n- and p-type doping concentrations n_0 and p_0 and the number of excited electron–hole pairs $\Delta n = \Delta p$. For a highly n-doped semiconductor, which yields $n_0 \gg \Delta n$, R_{rad} can be expressed as:

$$R_{\text{rad}} = B_{\text{rad}}(n_0 + \Delta n)(p_0 + \Delta p) \approx B_{\text{rad}}n_0\Delta p \quad (15)$$

The experimentally observed radiative lifetime τ_{rad} is determined by the recombination rate per volume R_{rad} and the number of excited electron–hole pairs $\Delta n = \Delta p$ such that $\tau_{\text{rad}} = \Delta p/R_{\text{rad}}$. Combining this result with equation (15) gives a definition for the *B*-coefficient of:

$$B_{\text{rad}} = \frac{1}{\tau_{\text{rad}}n_0} \quad (16)$$

In this equation, τ_{rad} is the radiative lifetime at 300 K and n_0 is the activated donor density. To determine the B_{rad} coefficient we carefully evaluate the determined values for τ_{rad} and the doping density n_0 .

The measured photoluminescence lifetimes show a spread over different wires as shown in the right panel of Fig. 4b. We attribute this spread to a variation of the optical density of states of each individual wire. Using the decay times measured at 4 K and extrapolating them to 300 K assuming temperature independence, we deduce an upper limit of 1.6 ns, while the lower limit is close to 0.4 ns, as shown by the 300 K measurements. Because it is of key importance that the measured lifetime is equal to the radiative lifetime we carefully address this point below.

(1) We might argue whether the measured photoluminescence decay time at 300 K is equal to the radiative lifetime. Our main argument is provided by the right panel of Fig. 4c, which shows that the photoluminescence intensity at 300 K is almost equal to the photoluminescence intensity at 4 K. Since we know that hex-SiGe is in the radiative limit at 4 K, and we observe almost the same emission intensity at 300 K, it is clear that hex-SiGe must remain very close to the radiative limit at 300 K.

(2) A second point of concern might be whether we are still in the degenerate limit $\Delta n < n_0$. The main evidence for this point is that, for most wires, we measure an excitation-power-independent photoluminescence decay time in the same excitation range as in the inset of Fig. 4c. In addition, we measure a temperature-independent photoluminescence lifetime in Fig. 4b (see the Methods section ‘Temperature dependence of the radiative lifetime’), which can only occur for a semiconductor with degenerate doping.

The donor density n_0 was estimated using two techniques, the first of which is APT, shown in Extended Data Fig. 6, where a donor concentration of $n_0 = 9 \times 10^{18} \text{ cm}^{-3}$ is found. However, this number might differ from the number of active dopants. The active doping concentration

Article

can be calculated from the electron quasi-Fermi level, as determined from the LSW fitting and the density of states in the conduction band, where a value of $n_0 = 3 \times 10^{18} \text{ cm}^{-3}$ is found. This model approach, however, should be considered a lower bound, as further discussed in the Methods section 'LSW model'. Now, combining the upper bound for the donor density of $9 \times 10^{18} \text{ cm}^{-3}$ with the upper bound of 1.6 ns for the radiative lifetime, we obtain a lower bound for the B -coefficient of $0.7 \times 10^{-10} \text{ cm}^3 \text{ s}^{-1}$. Using the lower limits for n_0 and τ_{rad} an upper limit of $8.3 \times 10^{-10} \text{ cm}^3 \text{ s}^{-1}$ is found for the B -coefficient. If we compare with other well known semiconductors such as GaAs, InP or cub-Si with B -coefficients of $3.5 \times 10^{-10} \text{ cm}^3 \text{ s}^{-1}$, $1.2 \times 10^{-10} \text{ cm}^3 \text{ s}^{-1}$ and $4.73 \times 10^{-15} \text{ cm}^3 \text{ s}^{-1}$, respectively, we observe that the B -coefficient of hex-SiGe is between $2\times$ smaller and $7\times$ larger than the B -coefficient of InP, whereas it is 4 to 5 orders of magnitude larger than the B -coefficient of cub-Si. Extracting the B -coefficient and thus the transition matrix elements is of great importance for possible device applications of hex-SiGe, such as lasers, modulators, detectors and LEDs, which all depend critically on the strength of the light–matter interaction.

External radiative efficiency of hex-SiGe

Here we estimate the external radiative efficiency of our hex-Si_{0.20}Ge_{0.80} nanowire shells by measuring the emitted photoluminescence intensity in the setup used to measure the photoluminescence lifetime, using a 1,030-nm laser source. To compare the external radiative efficiency with a standard, we measure the intensity obtained from our hex-SiGe shells and compare with high-quality InGaAs/InP multiple quantum well (MQW) samples. These samples are state-of-the art direct-bandgap materials for quantum well lasers^{81,82} and infrared photonic devices. These quantum wells are chosen to emit in a wavelength region similar to that of hex-Si_{0.20}Ge_{0.80} to eliminate any wavelength dependence of our detection system. The measured integrated photoluminescence intensities are presented in Extended Data Fig. 10a.

To compare the emission intensity of these very different optical structures, we first calculate the absorption probability of both structures when excited using light at 1,030 nm, as used in the main text. The MQW structure has 30% reflection loss at the surface. The effective absorption length and absorption coefficient are 625 nm (Extended Data Fig. 10b) and $\alpha \approx 10^5 \text{ cm}^{-1}$, resulting in 99.85% light absorption. The total absorption probability for the MQW sample is thus estimated to be 70%. The wires were mechanically transferred onto a silicon wafer which has a chromium (15 nm), Au (300 nm) and SiO_x (12 nm) top layer to act as a back mirror. We subsequently calculate the absorption using finite difference time domain methods using the Lumerical (<https://www.lumerical.com/>) software package. For a Gaussian beam with a beam waist of 5 μm , we calculate an absorption probability of 38% for the 7- μm -long hex-SiGe nanowire shell. Subsequently, we calculated the light emission probability into our Cassegrain objective with a numerical aperture (NA) = 0.48 and a NA = 0.22 obscurity both for the wires and the MQWs. For hex-SiGe, the light is polarized perpendicularly to the nanowire growth axis, which is the c axis, in the horizontal or vertical direction; see Extended Data Fig. 10c.

We calculate the emission intensity by randomly positioning 42 dipoles within the hex-SiGe nanowire shell in a vertically oriented cross-section and subsequently adding the emission from ten different cross-sections within the 5- μm laser spot. When we average the emission intensity collected by our objective over both the horizontal and the vertical polarization directions (see Extended Data Fig. 10c), we obtain a light collection probability of 0.35%. Therefore, correcting for the absorption and the collection probability, we find a correction factor for the hex-SiGe nanowires of $1/(0.38 \times 0.0035) = 7.5 \times 10^2$. Since the MQW samples have high internal quantum efficiency, we approximate the photon escape probability as being equal to the escape cone at the front surface, divided by the escape cone at the interface of the Q1.25 InGaAsP layer and InP. The escape cone is defined by the expression

$P_{\text{esc}} = \frac{1}{2}(1 - \cos\theta_{\text{critical}}) \approx \frac{1}{4}\left(\frac{n_{\text{cladding}}}{n_{\text{semiconductor}}}\right)^2$, which is 2.2% at the InGaAsP/air interface and 22% at the InGaAsP/InP interface, yielding an approximate photon escape probability in the MQW of 10%. Additionally, a Lambertian emission profile is assumed from the surface of the MQW, which results in an 18% collection probability in our Cassegrain objective, taking into account both the numerical aperture and the obscurity. We thus find a correction factor of $1/(0.70 \times 0.10 \times 0.18) = 79$ for the MQW. The corrected data for both the hex-SiGe nanowires and the MQWs are plotted together with the original data in Extended Data Fig. 10a. The important conclusion from Extended Data Fig. 10 is that the corrected emission from our hex-SiGe nanowire shells is of the same order of magnitude to our high-quality InGaAs/InP MQWs when their more complex three-dimensional dielectric geometry is corrected for. A more quantitative assessment of the external radiative efficiency, such as incorporating exciton-polaritons, is outside the scope of this work, but these simple considerations, combined with the experimental evidence presented in the main text, provide strong additional support for our conclusion that hex-SiGe is a direct-bandgap semiconductor with high internal radiative efficiency.

Comparison with previous generation hex-Ge nanowire shells

The evolution of the photoluminescence spectra for different growth recipes will be published on <https://doi.org/10.4121/uuid:68e75799-0378-4130-9764-b80cb1f2319b> as open datasets. Briefly, the spectra of hex-Ge were observed to be considerably broadened when the samples were grown using a wurtzite-GaP core nanowire as shown in Extended Data Fig. 11a. In addition, we were not able to observe a clear spectrum at room temperature. The photoluminescence spectra improved when we used wurtzite-GaAs core to grow the hex-Ge shell at temperatures of 600 °C and 650 °C, as shown in Extended Data Fig. 11b and c, respectively. Finally, an improvement of the photoluminescence was realized by using longer wurtzite-GaAs core nanowires, which yielded the spectra in Fig. 3a, b.

Data availability

All data underlying this study are available from the 4TU ResearchData repository at <https://doi.org/10.4121/uuid:68e75799-0378-4130-9764-b80cb1f2319b>.

39. Kresse, G. & Furthmüller, J. Efficient iterative schemes for ab initio total-energy calculations using a plane-wave basis set. *Phys. Rev. B* **54**, 11169–11186 (1996).
40. Perdew, J. P. et al. Restoring the density-gradient expansion for exchange in solids and surfaces. *Phys. Rev. Lett.* **100**, 136406 (2008).
41. Tran, F. & Blaha, P. Accurate band gaps of semiconductors and insulators with a semilocal exchange-correlation potential. *Phys. Rev. Lett.* **102**, 226401 (2009).
42. Borlido, P. et al. Large-scale benchmark of exchange-correlation functionals for the determination of electronic band gaps of solids. *J. Chem. Theory Comput.* **15**, 5069–5079 (2019).
43. Schleife, A., Rödl, C., Furthmüller, J. & Bechstedt, F. Electronic and optical properties of MgZnO and CdZnO from ab initio calculations. *New J. Phys.* **13**, 085012 (2011).
44. Kriegner, D., Wintersberger, E. & Stangl, J. xrayutilities: A versatile tool for reciprocal space conversion of scattering data recorded with linear and area detectors. *J. Appl. Cryst.* **46**, 1162–1170 (2013).
45. Kölling, S. et al. Atom-by-atom analysis of semiconductor nanowires with parts per million sensitivity. *Nano Lett.* **17**, 599–605 (2017).
46. Kölling, S. et al. Impurity and defect monitoring in hexagonal Si and SiGe nanocrystals. *ECS Trans.* **75**, 751–760 (2016).
47. Jacobsson, D. et al. Phase transformation in radially merged wurtzite GaAs nanowires. *Cryst. Growth Des.* **15**, 4795–4803 (2015).
48. Alexander, M. N. & Holcomb, D. F. Semiconductor-to-metal transition in n-type group IV semiconductors. *Rev. Mod. Phys.* **40**, 815 (1968).
49. Chen, H. L. et al. Determination of n-type doping level in single GaAs nanowires by cathodoluminescence. *Nano Lett.* **17**, 6667–6675 (2017).
50. Katahara, J. K. & Hillhouse, H. W. Quasi-Fermi level splitting and sub-bandgap absorptivity from semiconductor photoluminescence. *J. Appl. Phys.* **116**, 173504 (2014).
51. Einstein, A. Zur Quantentheorie der Strahlung. *Phys. Z.* **18**, 361–391 (1917).
52. Ortolani, M. et al. Long intersubband relaxation times in n-type germanium quantum wells. *Appl. Phys. Lett.* **99**, 201101 (2011).
53. Virgilio, M. et al. Modeling picosecond electron dynamics of pump-probe intersubband spectroscopy in n-type Ge/SiGe quantum wells. *Phys. Rev. B* **86**, 205317 (2012).

54. Virgilio, M. et al. Combined effect of electron and lattice temperatures on the long intersubband relaxation times of Ge/Si_xGe_{1-x} quantum wells. *Phys. Rev. B* **89**, 045311 (2014).
55. Klingshirn, C. F. *Semiconductor Optics* (Springer, 2012).
56. Green, M. A. Intrinsic concentration, effective densities of states, and effective mass in silicon. *J. Appl. Phys.* **67**, 2944–2954 (1990).
57. Varshni, Y. P. Temperature dependence of the energy gap in semiconductors. *Physica* **34**, 149–154 (1967).
58. Viña, L., Logothetidis, S. & Cardona, M. Temperature dependence of the dielectric function of germanium. *Phys. Rev. B* **30**, 1979–1991 (1984).
59. Polimeni, A. et al. Effect of temperature on the optical properties of (InGa)(AsN)/GaAs single quantum wells. *Appl. Phys. Lett.* **77**, 2870 (2000).
60. Reschchikov, M. A. Temperature dependence of defect-related photoluminescence in III-V and II-VI semiconductors. *J. Appl. Phys.* **115**, 012010 (2014).
61. Leroux, M. et al. Temperature quenching of photoluminescence intensities in undoped and doped GaN. *J. Appl. Phys.* **86**, 3721 (1999).
62. Bacher, G. et al. Influence of barrier height on carrier dynamics in strained In_xGa_{1-x}As/GaAs quantum wells. *Phys. Rev.* **B43**, 9312–9315 (1991).
63. Lourenço, S. A. et al. Effect of temperature on the optical properties of GaAsSbN/GaAs single quantum wells grown by molecular-beam epitaxy. *J. Appl. Phys.* **93**, 4475–4479 (2003).
64. Schenk, H. P. D., Leroux, M. & De Mierry, P. Luminescence and absorption in InGaN epitaxial layers and the van Roosbroeck-Shockley relation. *J. Appl. Phys.* **88**, 1525–1534 (2000).
65. Lambkin, J. D. et al. Temperature dependence of the photoluminescence intensity of ordered and disordered In_{0.48}Ga_{0.52}P. *Appl. Phys. Lett.* **65**, 73–75 (1994).
66. Feldmann, J. et al. Dependence of radiative exciton lifetimes in quantum. *Phys. Rev. Lett.* **59**, 2337–2340 (1987).
67. 'tHooft, G. W., van der Poel, W. A. J. A., Molkenkamp, L. W. & Foxon, C. T. Giant oscillator strength of free excitons in GaAs. *Phys. Rev. B* **35**, 8281–8284 (1987).
68. Bellessa, J. et al. Quantum-size effects on radiative lifetimes and relaxation of excitons in semiconductor nanostructures. *Phys. Rev. B* **58**, 9933–9940 (1998).
69. Jiang, N. et al. Long minority carrier lifetime in Au-catalyzed GaAs/Al_xGa_{1-x}As core-shell nanowires. *Appl. Phys. Lett.* **101**, 023111 (2012).
70. Virgilio, M. et al. Radiative and non-radiative recombination in tensile strained Ge microstrips: photoluminescence experiments and modeling. *J. Appl. Phys.* **118**, 233110 (2015).
71. Schubert, E. F. *Light-Emitting Diodes* (Cambridge Univ. Press, 2006).
72. Benz, G. & Conradt, R. Auger recombination in GaAs and GaSb. *Phys. Rev. B* **16**, 843–855 (1977).
73. Galler, B. et al. Experimental determination of the dominant type of Auger recombination in InGaN quantum wells. *Appl. Phys. Express* **6**, 112101 (2013).
74. Haug, A., Kerkhoff, D. & Lochmann, W. Calculation of Auger coefficients for III-V semiconductors with emphasis on GaSb. *Phys. Status Solidi* **89**, 357–365 (1978).
75. 't Hooft, G. W., Leys, M. R. & Talen-v.d. Mheen, H. J. Temperature dependence of the radiative recombination coefficient in GaAs-(Al, Ga)As quantum wells. *Superlatt. Microstruct.* **1**, 307–310 (1985).
76. Mayer, B. et al. Monolithically integrated high-β nanowire lasers on silicon. *Nano Lett.* **16**, 152–156 (2016).
77. Drexhage, K. H., Kuhn, H. & Schäfer, F. P. Variation of the fluorescence decay time of a molecule in front of a mirror. *Phys. Chem. Chem. Phys.* **72**, 329 (1968).
78. Drexhage, K. H. Influence of a dielectric interface on fluorescence decay time. *J. Lumin.* **1–2**, 693–701 (1970).
79. Yoo, Y. S., Roh, T. M., Na, J. H., Son, S. J. & Cho, Y. H. Simple analysis method for determining internal quantum efficiency and relative recombination ratios in light emitting diodes. *Appl. Phys. Lett.* **102**, 211107 (2013).
80. Schmidt, T., Lischka, K. & Zulehner, W. Excitation-power dependence of the near-band-edge photoluminescence of semiconductors. *Phys. Rev. B* **45**, 8989–8994 (1992).
81. D'Agostino, D. et al. Monolithically integrated widely tunable coupled cavity laser source for gas sensing applications around 2.0 μm wavelength. In *Advanced Photonics OSA Technical Digest Paper JT5A.1* (Optical Society of America, 2015).
82. Latkowski, S. et al. Monolithically integrated widely tunable laser source operating at 2 μm. *Optica* **3**, 1412–1417 (2016).
83. Assali, S. et al. Growth and optical properties of direct band gap Ge/Ge_{0.87}Sn_{0.13} core/shell nanowire arrays. *Nano Lett.* **17**, 1538–1544 (2017).
84. Kumar, A. et al. On the interplay between relaxation, defect formation, and atomic Sn distribution in Ge_(1-x)Sn_(x) unraveled with atom probe tomography. *J. Appl. Phys.* **118**, 025302 (2015).

Acknowledgements We thank D. Buca, A. Polimeni, J. de Boeck and C. Palmstrøm for discussions. We thank R. van Veldhoven for the technical support of the MOVPE reactor and providing the MQW samples. We acknowledge DESY (Hamburg, Germany), a member of the Helmholtz Association HGF, for the provision of experimental facilities. Parts of this research were carried out at PETRA III and we thank F. Bertram for assistance in using beamline P08. This project received funding from the European Union's Horizon 2020 research and innovation program under grant agreement number 735008 (SiLAS), the Dutch Organization for Scientific Research (NWO) and from a Marie Skłodowska-Curie Action fellowship (GA number 751823). We acknowledge Soliance, a solar energy R&D initiative of ECN, TNO, Holst, TU/e, imec, Forschungszentrum Jülich, and the Dutch province of Noord-Brabant for funding the TEM facility. We thank the Leibniz Supercomputing Centre for providing computational resources on SuperMUC (project number pr62ja).

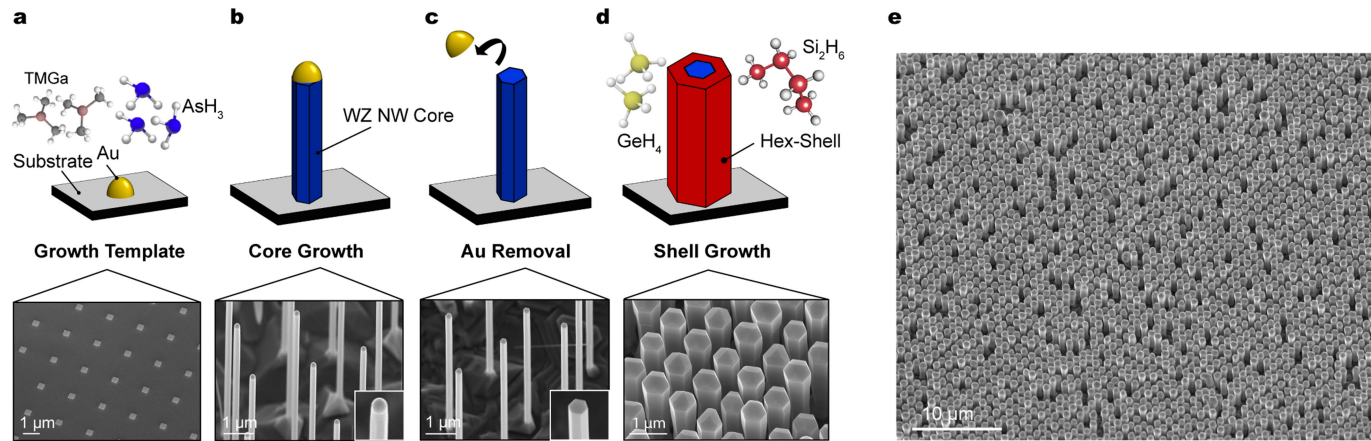
Author contributions E.M.T.F., C.M. and Y.R. carried out the growth of wurtzite nanowire cores. E.M.T.F. carried out the growth of hex-SiGe shells and analysed the data. A.D. and D.B. carried out the photoluminescence spectroscopy. A.D. analysed the optical data. M.A.J.V.T., A.D. and V.T.v.L. performed time-resolved spectroscopy on single nanowires; K.K. performed optical finite difference time domain simulations. J.R.S., C.R., J.F. and S.B. performed the DFT calculations. D.Z. and J.S. performed the XRD measurements. S.K. performed the APT characterization. M.A.V. performed the TEM analysis. J.R.S., J.F., S.B., J.E.M.H. and E.P.A.M.B. supervised the project. F.B. contributed to the interpretation of data and E.M.T.F., A.D., D.Z., S.B., J.J.F., J.E.M.H. and E.P.A.M.B. contributed to the writing of the manuscript. All authors discussed the results and commented on the manuscript.

Competing interests The authors declare no competing interests.

Additional information

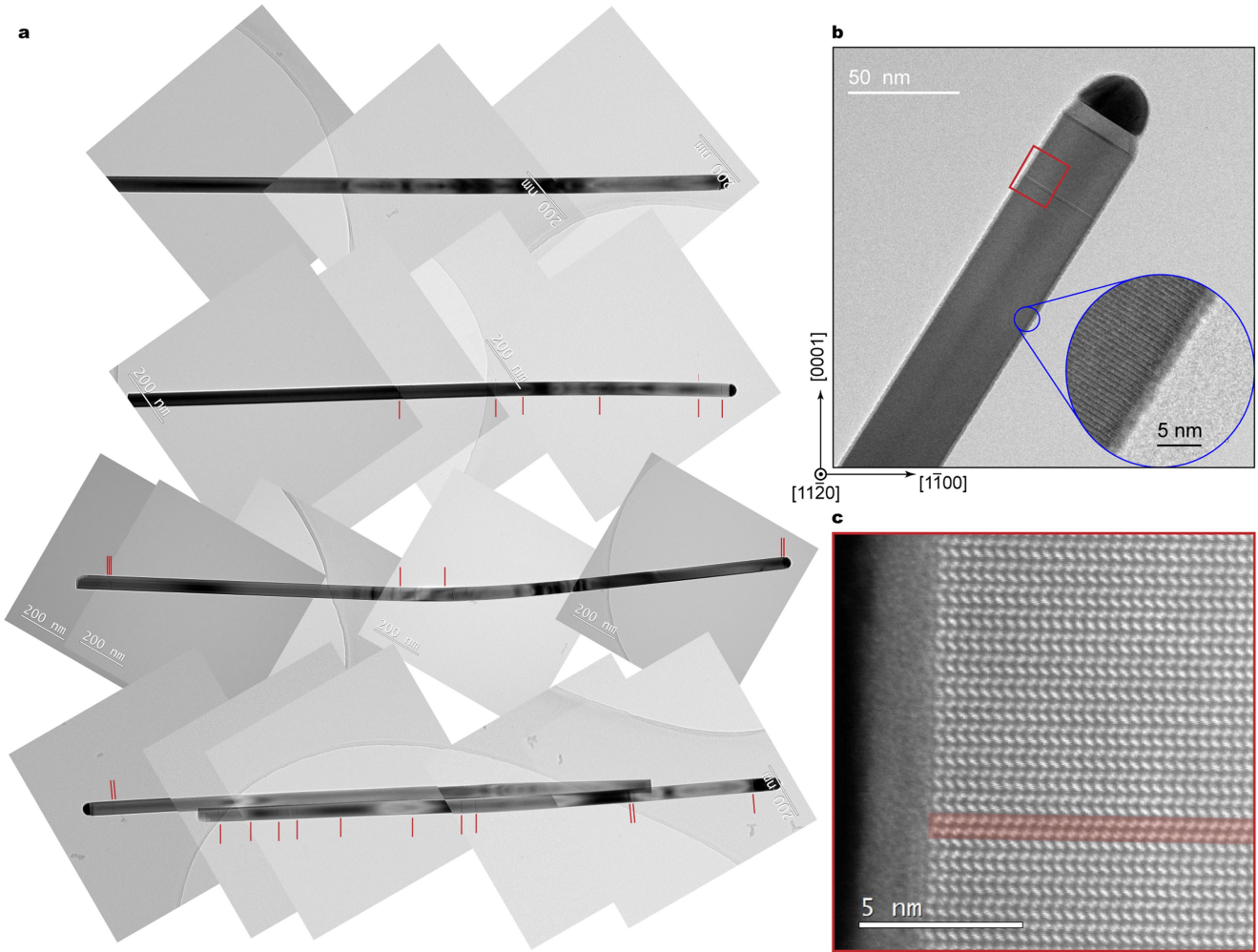
Correspondence and requests for materials should be addressed to E.P.A.M.B.

Reprints and permissions information is available at <http://www.nature.com/reprints>.



Extended Data Fig. 1 | Schematic illustration of the nanowire growth process. **a**, The core nanowire growth starts with a GaAs (111)B substrate patterned with Au catalyst seeds, which is introduced in the MOVPE reactor and annealed at a temperature higher than the eutectic temperature forming an alloy between the catalyst seed and the substrate. **b**, Next, the GaAs gas precursors (TMGa and AsH₃) are introduced, and Au-catalysed GaAs core nanowires are grown. To proceed with the SiGe shell growth, Au seeds are chemically etched away from the GaAs cores and the surface of the cores is repaired (**c**), and the sample is reintroduced to the MOVPE reactor (**d**).

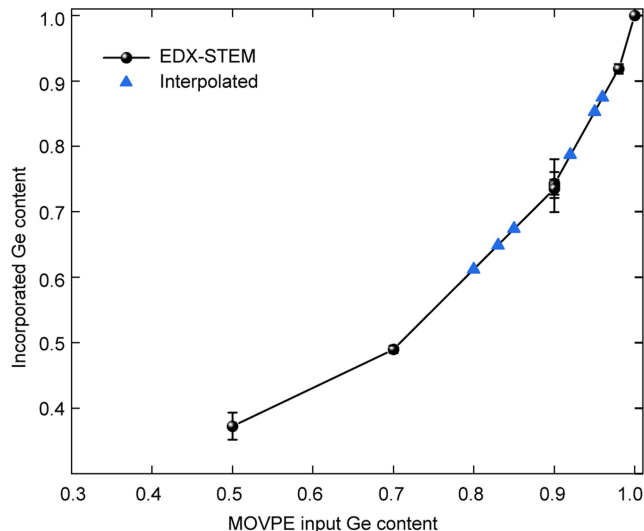
A hex-Si_{1-x}Ge_x shell is epitaxially grown around the GaAs cores from precursors (Si₂H₆ and GeH₄). (The molecules are drawn with the freely available MolView Software (<http://www.molview.org/>)). The 30° tilted scanning electron microscopy images in the bottom panels of **a–d** are representative of the results of the growth steps in the top panels, with insets in **b** and **c** displaying a magnified image of the nanowire. **e**, A 30° tilted-overview representative scanning electron microscopy image of hex-Ge/GaAs Core shells corresponding to what is shown in Fig. 2, confirming the uniformity of the growth across the sample.



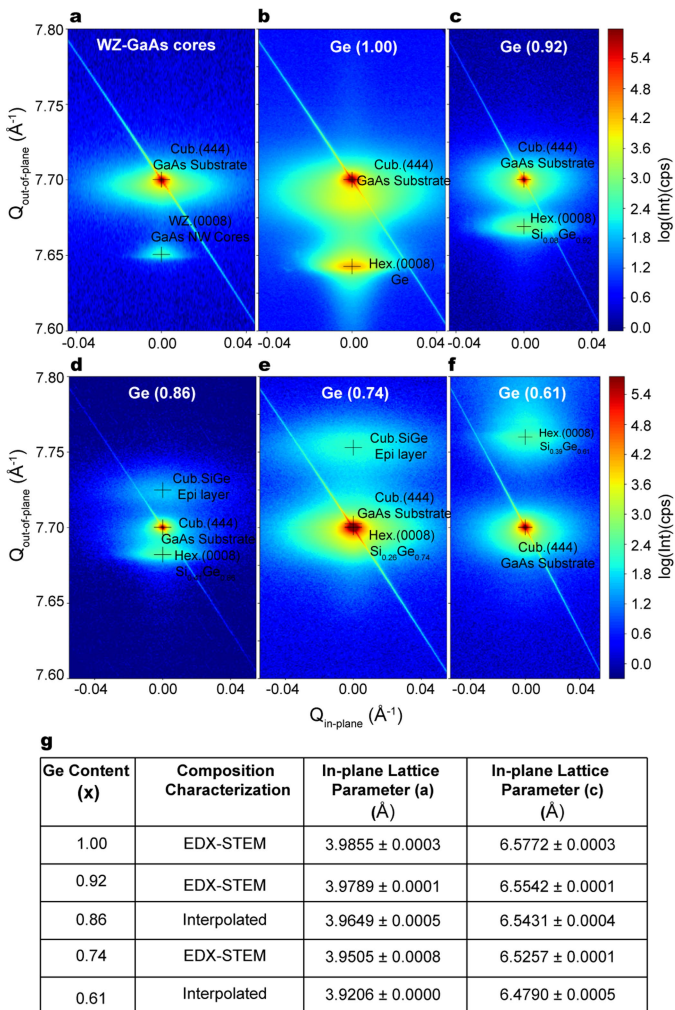
Extended Data Fig. 2 | Crystal quality of the wurtzite GaAs nanowire cores.
a, Bright-field TEM images recorded in the $[11\bar{2}0]$ zone axis of five representative GaAs core nanowires of a pure wurtzite crystal (stacking faults indicated with red lines), with a stacking-fault density of 0–6 stacking faults per micrometre.
b, A zoomed-in bright-field TEM image of the top part of one of the nanowires in

a (blue circle), indicating the purity of the crystal structure. **c**, HAADF-STEM image of the red box in **b**, displaying the ABAB stacking of the GaAs atomic columns, which is the hallmark of the hexagonal crystal structure. The red shading highlights a stacking fault forming one cubic layer in the hexagonal structure.

Article

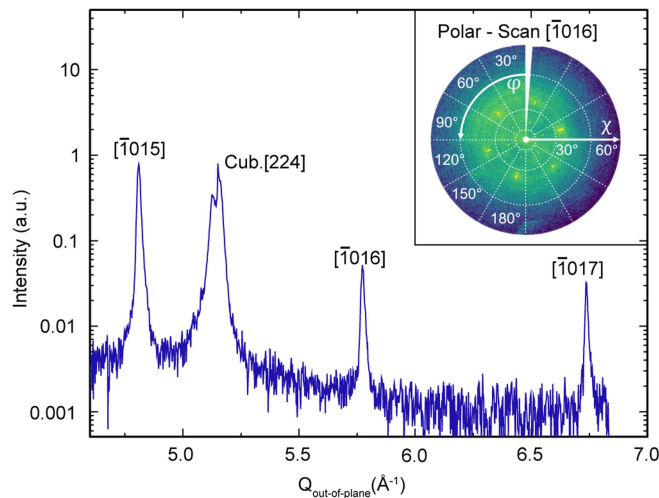


Extended Data Fig. 3 | Ge content calibration curve. A calibration curve for the incorporated atomic fraction of Ge in the as-grown SiGe shells discussed in Fig. 2e, f and Fig. 5. Owing to growth kinetics, the input percentage of gas precursors in the MOVPE reactor does not always match the actual incorporated atomic percentage in the grown $\text{Si}_{1-x}\text{Ge}_x$ shell structures. To map the compositional output onto the input Ge fraction, the real content of four $\text{Si}_{1-x}\text{Ge}_x$ shells was measured by EDX-STEM and plotted as solid black circles. The compositions of additional samples were determined based on their input Ge fraction by interpolating the EDX-STEM data points and are indicated by blue triangles. The error bars for the black data points represent the standard deviation in the composition across three different analysed nanowires per sample. The accuracy of EDX in STEM is confirmed by determining the composition of a single sample, corresponding to MOVPE input $\text{Si}_{0.10}\text{Ge}_{0.90}$, with both EDX-STEM and APT. The APT data is shown in Extended Data Fig. 6 and was performed on three different nanowires. Both techniques yielded almost the same Ge composition—0.74 and 0.75 respectively—which is within the standard deviation across the whole sample. The reproducibility of this calibration method is also confirmed by photoluminescence, where almost identical spectra are observed for two different samples grown with the same input.

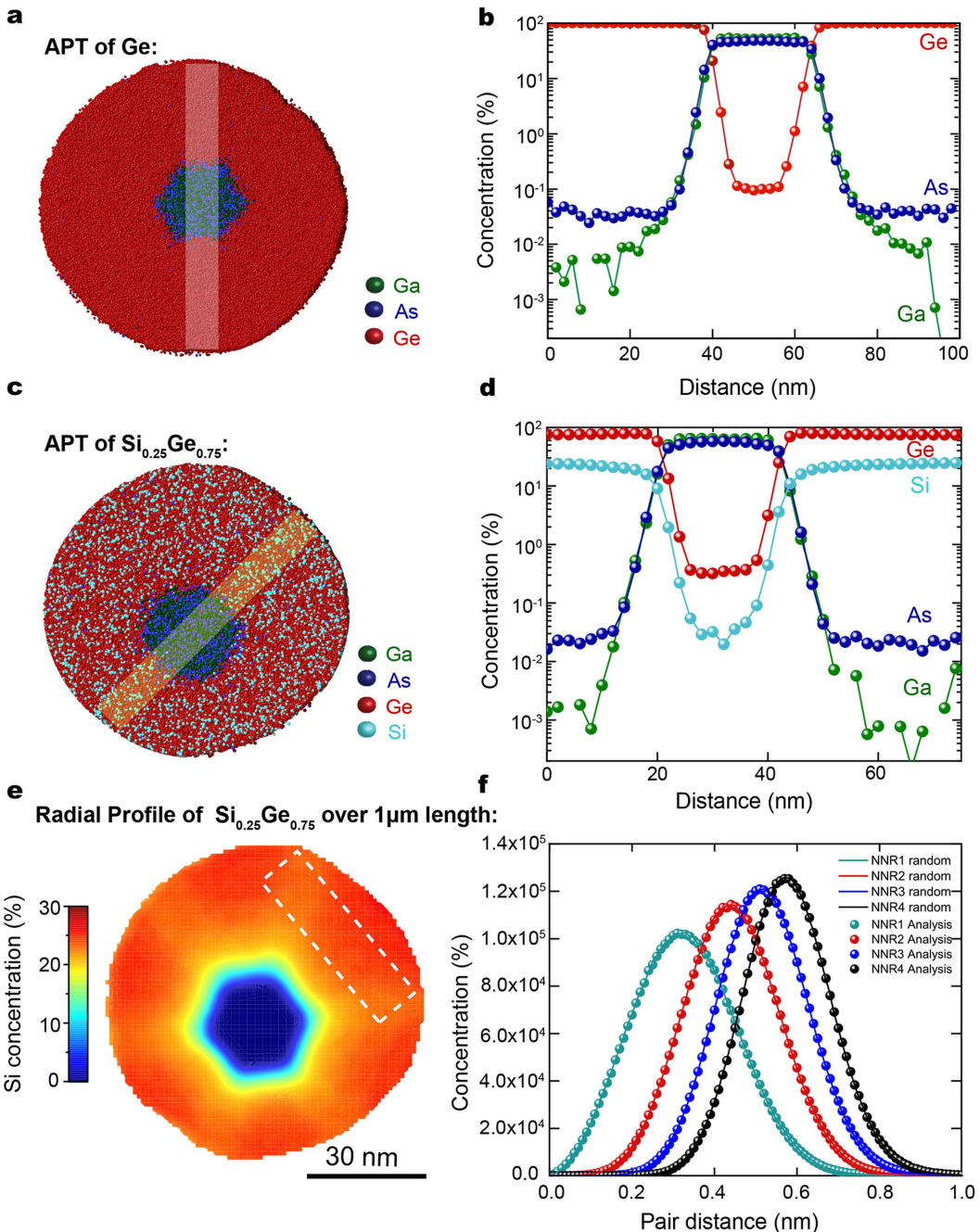


Extended Data Fig. 4 | Full series of symmetric (0008) reflections of hex-Si_{1-x}Ge_x. **a**, An RSM of as-grown wurtzite GaAs nanowires on a cub-GaAs substrate, containing the wurtzite-GaAs (0008) reflection and the cub-GaAs (444) reflection. **b**, An RSM for a sample similar to that in **a** but with a thick Ge shell, including the cub-GaAs (444) substrate reflection and the hex-Ge (0008) reflection. **c–f**, Additional RSMs are shown for samples with Si_{1-x}Ge_x shells, for x = 0.92 (**c**), for x = 0.86 (**d**), for x = 0.74 (**e**) and for x = 0.61 (**f**). The intensities (Int) of the reflections are colour-coded on a logarithmic scale, in units of counts per second (cps). A clearly increasing shift of Q_{out-of-plane} can be observed for increasing Si content, corresponding to a decreasing lattice constant. For the RSMs in **d** and **e** a reflection from a parasitic, epitaxial cub-SiGe layer is also found. **g**, Tabulated hexagonal lattice parameters of all measured hex-Si_{1-x}Ge_x samples with corresponding error values extracted from XRD measurements. The errors given take into account the accuracy of defining the peak position with a two-dimensional fit as described, as well as the scattering of the individual lattice parameter values extracted from the evaluation of multiple peaks. EDX-STEM was used to determine the composition of some samples and the rest were interpolated on the basis of the curve in Extended Data Fig. 3.

Article

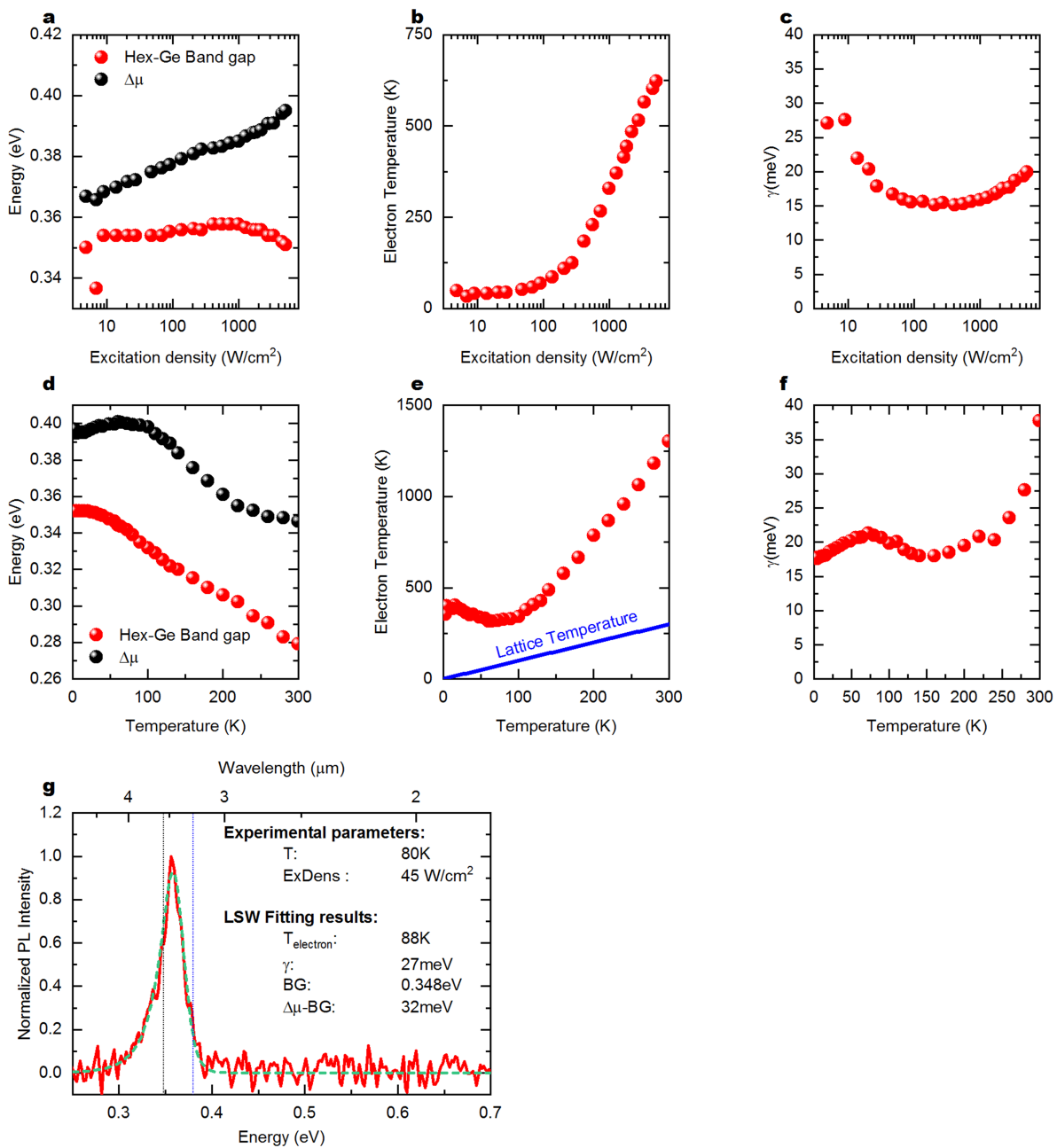


Extended Data Fig. 5 | Crystal-truncation-rod scan and polar scan. For a representative sample with $\text{Si}_{0.20}\text{Ge}_{0.80}$ shells and a GaAs core, a scan along the asymmetric $[\bar{1}01\text{L}]$ nanowire crystal truncation rod is shown, covering a total of three wurtzite reflections, $[\bar{1}015]$, $[\bar{1}016]$ and $[\bar{1}017]$. L refers to a crystallographic coordinate according to the HKiL Miller-Bravais ($i = -(H + L)$) index notation. In addition, also the cubic [224] substrate reflection and the parasitic cub-SiGe epilayer is visible (as a double-peak feature around the [224] reflection). In between the wurtzite reflections no additional reflections are visible, which indicates that only the pure wurtzite 2H phase is present in the nanowire system. The inset shows an XRD polar scan around the $[\bar{1}016]$ reflection, confirming the six-fold symmetry of the wurtzite lattice. Each reflection, seen in the polar scan, is separated by a sample rotation of exactly 60° from the next reflection (φ rotation axis, χ tilt axis). The absence of additional Bragg reflections in between indicates a pure wurtzite phase and high crystal quality.



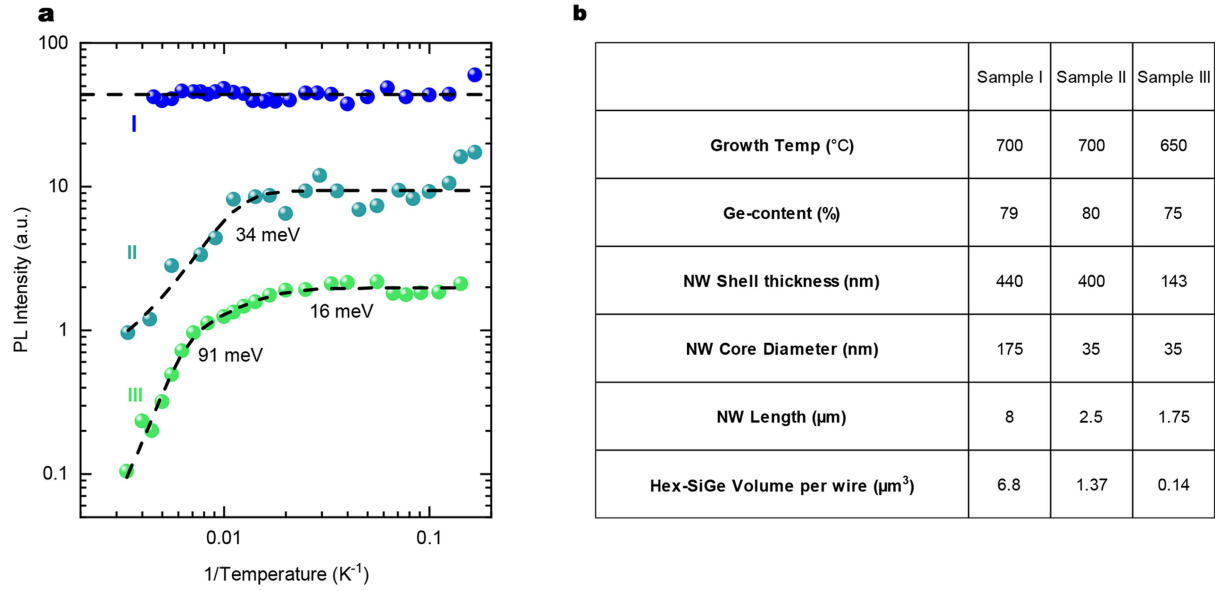
Extended Data Fig. 6 | APT characterization of hex-Ge and $\text{Si}_{0.25}\text{Ge}_{0.75}$. **a, c,** Ge (red) and Si (cyan) is shown to form a shell around the hexagonal Ga (green) and the As (blue) core. **a.** A three-dimensional volume reconstruction of part of a hex-GaAs/Ge core/shell nanowire with thicknesses of 35 nm/80 nm. For clarity, only a slab of 50 nm thickness of the entire 1.4- μm -long analysis is shown. **c.** A three-dimensional volume reconstruction of part of a hex-GaAs/ $\text{Si}_{0.25}\text{Ge}_{0.75}$ core/shell nanowire with thicknesses of 35 nm/46 nm. For clarity, only a slab of 40 nm thickness of the entire 1.1- μm -long analysis is shown. **b, d,** A plot of the atomic species concentration in the Ge ($\text{Si}_{0.25}\text{Ge}_{0.75}$) shell in the rectangles in **a** (white) and **c** (yellow) as a function of the radial distance across the core/shell structure. Every data point in the plot represents a 2-nm slice taken along the entire length of the nanowire analyses excluding the cubic top part of the nanowire. Constant incorporation of As at a level of approximately

400 parts per million (**b**) (200 parts per million (**d**)) is observed in the entire shell while the Ga concentration quickly drops to a value close to the noise level of -10 parts per million. **e.** A radial profile of the SiGe core/shell structure from the APT measurement integrated over a 1.0- μm length of the structure showing a Ge content of around 0.75 as shown in **d**. On the dotted rectangular volume of **e**, we carry out a nearest-neighbour analysis for Si atoms as previously used to evaluate random alloys of GeSn^{83,84}. The nearest-neighbour analysis evaluates the distances between each pair of Si atoms and its first (to fourth) neighbours (NN1 to NN4). **f.** In **b** and **d** and **f**, the atomic concentration of the individual elements is plotted in the volume of the shaded regions indicated in **a**, **c** and **e**. A plot comparing the nearest-neighbour analysis on the measurement data to a randomized dataset. This gives us no indication of Si clustering and has been established as a reliable way to evaluate random alloys⁴⁶.

**Extended Data Fig. 7 | LSW fit of photoluminescence-spectra on hex-Ge.**

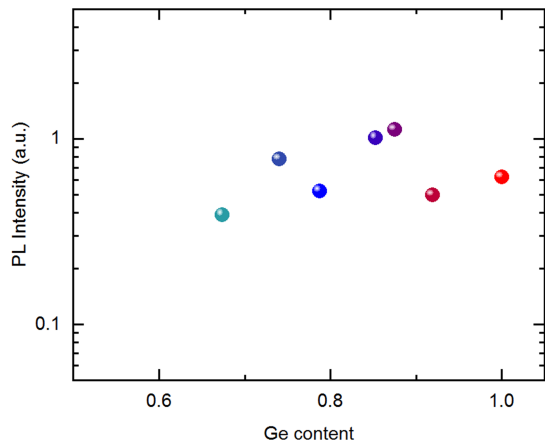
LSW fits were performed both on low-temperature (4 K), excitation-density-dependent photoluminescence spectra of hex-Ge as plotted in Fig. 3a, as well as on a temperature series of photoluminescence spectra of hex-Ge at an excitation density of 1.8 kW cm^{-2} as plotted in Fig. 3b. Additional fitting results are given here, with a full description of the model given in the Methods section ‘The LSW model’. **a, d**, The bandgap and the quasi-Fermi-level splitting as a function of excitation density and temperature, respectively. **b, e**, The electron temperature as function of excitation density and temperature, respectively.

c, f, The Urbach-tail coefficient γ also as a function of excitation density and temperature, respectively. **g**, An LSW fit, plotted as a dashed green line, which was performed on a low-excitation-density (ExDens) (45 W cm^{-2}) photoluminescence spectrum, plotted as a red line, at a temperature of 80 K. Two vertical dotted lines indicate the bandgap (BG) on the left in black and the quasi-Fermi-level splitting $\Delta\mu$ to the right in blue. At this lattice temperature all dopants are ionized and the $\Delta\mu$ equals the electron-Fermi level, so these numbers are used to determine the electron quasi-Fermi level.

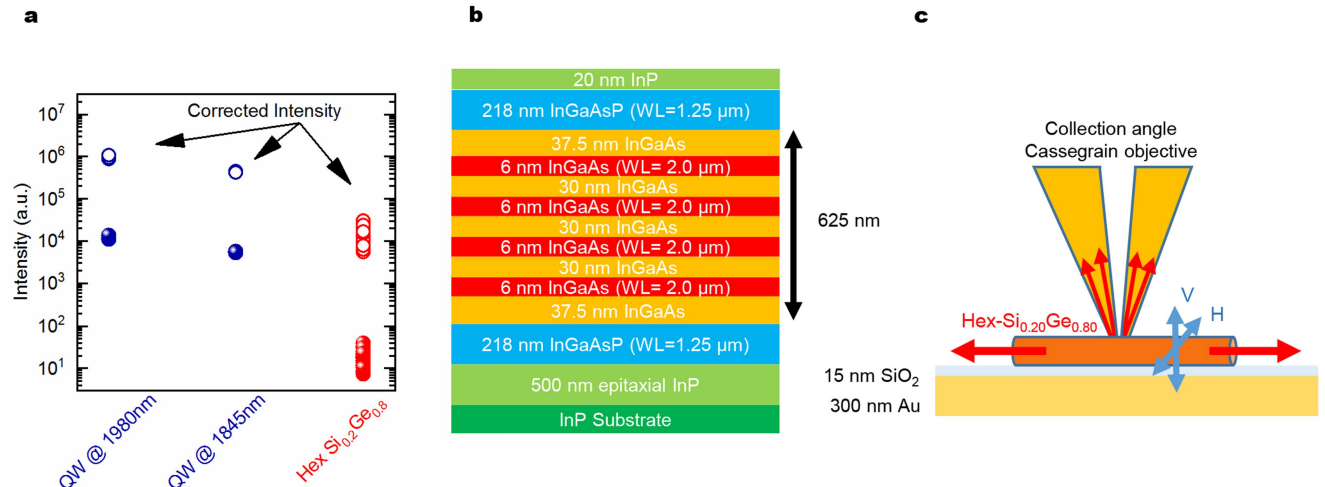


Extended Data Fig. 8 | Arrhenius plots of hex-Si_{0.20}Ge_{0.80} with varying quality and their growth parameters. **a**, The plots show the same data as presented in the left panel of Fig. 4c, but here presented in an Arrhenius representation. For the lowest-quality sample III, two non-radiative processes are found with activation energies of 16 meV and 91 meV. For sample II only a single activation energy is found, of 34 meV, whereas sample I does not show any decay in intensity over the full measured temperature range. The photoluminescence intensities at 4 K are proportional to the absorption cross-sections, which scale approximately with the volume fractions of the samples

that fit within the 5-μm-diameter laser spot. The volume ratios are 1:0.32:0.033 for samples I:II:III, respectively, where only 5/8 of the volume of sample I was counted (see Extended Data Fig. 8b). The measured photoluminescence intensities extrapolated to 4 K are proportional to 1:0.3:0.04 for the same samples, closely agreeing with the probed volumes. **b**, Tabulated growth parameters of the three different hex-SiGe samples studied, with increasing quality and the dimensions of the nanowires presented in Fig. 4b, c. The total diameter is the core diameter plus twice the shell thickness.

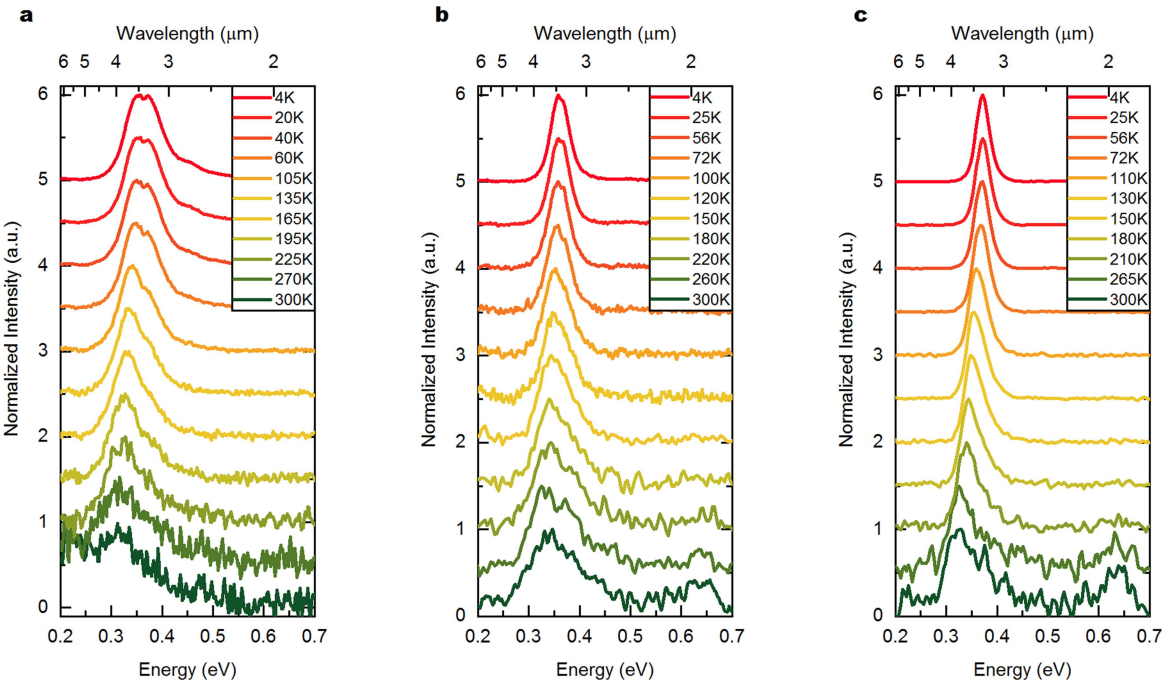


Extended Data Fig. 9 | Relative photoluminescence intensity between compositions. Here the relative photoluminescence intensities are given for the samples presented in Fig. 5. We note that only measurements on ensembles of as-grown standing wires are included where an equal number of wires is probed, and so the $\text{Si}_{0.35}\text{Ge}_{0.65}$ sample is not included. For this comparison all the samples were excited with an excitation density of 5 kW cm^{-2} at a temperature of 4 K using the same MCT detector and the same KBr beamsplitter. The samples are found to be very similar in intensity despite the change in setup efficiency, a variation in total excited volume due to thickness differences and potentially strain-induced nonradiative recombination centres for high Si-content samples. Because of these additional factors, no conclusive experimental argument can be made on whether the material becomes more efficient for higher Si contents. Additionally, we acknowledge that, despite efforts, we have not been able to measure photoluminescence spectra from wires with $x < 0.65$, which suggests that the direct–indirect-bandgap transition lies near this point.



Extended Data Fig. 10 | External radiative efficiency. **a**, Integrated photoluminescence intensities of hex-SiGe in comparison with high-quality InGaAs/InP multiple quantum well (QW) samples as measured in a micro-photoluminescence setup using 1,030-nm wavelength, 125-pJ pulses. The photoluminescence intensities of both the MQWs and the hex-SiGe wires were corrected using their respective absorption and emission efficiencies as given in the Methods section ‘External radiative efficiency of hex-SiGe’. **b**, A cross-

sectional schematic demonstrating the layer structure of the InGaAs/InP multiple QW sample, showing a total absorption thickness of 625 nm. The bandgap wavelengths (WL) of the layers that are not lattice-matched to InP are indicated. **c**, A schematic illustration of the geometry of our horizontally oriented hex-SiGe nanowire, showing the emission into a NA = 0.48 cassegrain objective with a NA = 0.22 obscenity. The polarization of the emitted light is indicated as V and H for vertical and horizontal, respectively.



Extended Data Fig. 11 | Comparison between different generations of hex-Ge samples. **a**, Photoluminescence spectra from the first hex-Ge shells, which were grown using wurtzite-GaP cores, thus creating many defects caused by the large lattice mismatch between the core and the shell. **b**, The first hex-Ge

shells grown on lattice-matching GaAs cores where the hex-Ge is grown at a temperature of 600 °C. **c**, Spectra of hex-Ge shells grown at a temperature of 650 °C, further improving the optical quality.